Nucleic Acids Research, 2026, **54**, gkag202
https://doi.org/10.1093/nar/gkag202
Molecular and Structural Biology

Bacillus subtilis ParB C-terminal lysine residues are essential for dimerization and *in vivo* function, indicating their roles in DNA sliding

Aleksey Aleshintsev [1,†], Lindsey E. Way [2,†], Ngoc Khanh Lai [2], Bianca Guerra [1,3], Paloma Dorantes [1], Lois Akosua Serwaa [4], Sealtiel Anulao [4], Miranda Molina [1,4], Xindan Wang [2,*], HyeongJun Kim [1,*]

[1]Department of Physics and Astronomy, University of Texas Rio Grande Valley, Edinburg, TX 78539, United States
[2]Department of Biology, Indiana University, Bloomington, IN 47405, United States
[3]Department of Biochemistry and Biophysics, Texas A&M University, College Station, TX 77840, United States
[4]School of Integrative Biological and Chemical Sciences, University of Texas Rio Grande Valley, Edinburg, TX 78539, United States

*To whom correspondence should be addressed. Email: hyeongjun.kim@utrgv.edu
Correspondence may also be addressed to Xindan Wang. Email: xindan@iu.edu
†The first two authors should be regarded as Joint First Authors.

Abstract

The broadly conserved ParB protein performs crucial functions in bacterial chromosome segregation and replication regulation. The cellular function of ParB requires it to dimerize, recognize *parS* DNA sequences, clamp on DNA, then slide to adjacent sequences through nonspecific DNA binding. How ParB coordinates nonspecific DNA binding and sliding remains elusive. Here, we combine multiple *in vitro* biophysical and computational tools and *in vivo* approaches to address this question. We found that five conserved lysine residues in the C-terminal domain (CTD) of ParB play distinct roles. While the two central rigid lysine residues provide the structural platform for the CTD, the three peripheral flexible lysine residues are implicated in efficient ParB sliding. Mutations in each individual lysine decreased ParB's DNA compaction capabilities, indicating that all five lysine residues are critical for properly positioning the DNA along the ParB CTD surface. Importantly, the integrity of these five lysines is crucial for ParB's *in vivo* functions, including fluorescence foci formation and sporulation initiation. Many proteins with diverse cellular activities need to move along DNA while loosely bound. Our findings provide molecular insight into how the fast backbone dynamics of multiple basic residues enable DNA-binding proteins to efficiently slide along DNA.

Graphical abstract

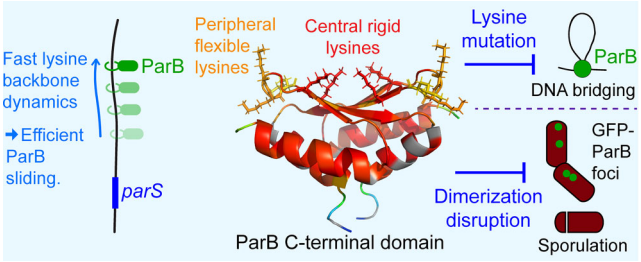

Introduction

Accurate chromosome replication and segregation are essential for all living organisms. For most bacterial chromosomes, this task is performed by a well-conserved ParABS system. ParA is a Walker-type ATPase that binds non-specifically to DNA [1, 2]; ParB is a CTPase that binds to the centromere-like *parS* DNA sequences, which are present as one or multiple copies in the vicinity of the origin of replication [3–5]. ParB stimulates the ATP hydrolysis of ParA, and repeated cycles of ParA and ParB interactions promote the segregation of the newly replicated origins [6–9]. ParB has a separate function in loading the structural maintenance of chromosomes (SMC) complexes onto the chromosome, which is also important for chromosome segregation [10, 11]. Finally, ParA's ATPase cycle regulates the initiation of DNA replication [12]. Therefore, the ParABS system plays an instrumental role in the segregation and replication of bacterial chromosomes [13, 14].

Received: July 10, 2025. **Revised:** February 16, 2026. **Accepted:** February 17, 2026

In some bacterial species, such as *Caulobacter crescentus*, the ParB protein is essential for cell viability [15]. In *Bacillus subtilis*, cells lacking *parB (*also known as *spo0J*) are viable in vegetative growth but exhibit a 50–100-fold increase in anucleate cells [16], emphasizing ParB's contribution to faithful chromosome segregation. In addition, ParB is required for sporulation, which is a developmental procedure *B. subtilis* undergoes under starvation and other stresses [16, 17].

ParB proteins have three conserved structural domains (Supplementary Fig. S1A) [13]. The N-terminal domain (NTD) (or the ParB/Srx domain) contains cytidine triphosphate (CTP) binding motifs [18–23] and ParA interaction domains [1, 24–26]. A recent study implies that NTD also mediates ParB multimerization and the formation of phase-separated condensate [23, 27]. The central DNA-binding domain (CDBD) specifically recognizes *parS* DNA sequences through its helix-turn-helix motif [20, 21, 28–31]. Preceded by a linker region, the C-terminal domain (CTD) is essential for nonspecific DNA binding [32, 33], ParB dimerization [21, 28, 34], and DNA condensation via ParB–ParB bridging interactions [33]. Nonspecific interactions with the negatively charged DNA backbone imply the presence of positively charged amino acids on the CTD across a wide range of ParB proteins (Supplementary Fig. S1B). Notably, a CTD nuclear magnetic resonance (NMR) structure (PDB: 5NOC) revealed a surface-exposed lysine-rich DNA-binding patch in *B. subtilis* [33].

ParB proteins bind not only at their cognate *parS* DNA binding sites but also in the 10–20 kb vicinity of each *parS* site [4, 34–36], a phenomenon termed spreading. Earlier models proposed a 1D filament-like spreading [4, 34, 36], where ParB polymerizes along DNA to form a continuous filament after loading on *parS*. This model was backed up by the observation of ParB spreading being attenuated by a protein "roadblock" positioned on one side of *parS* [36, 37]. However, quantitative immunoblots and fluorescence microscopy in *B. subtilis* estimated that the 1D filament model alone can account for only ∼500 bp (instead of 10–20 kb) of spreading due to the low ParB concentration (∼20 per *parS* site) [38]. The authors demonstrated that ParB proteins are capable of compacting flow-stretched DNA and proposed that DNA bridging events are required for ParB spreading [38]. Later, Sanchez and coworkers discovered that a majority of ParB molecules are localized around *parS* and proposed a nucleation and caging model [39]. The paradigm-shifting discoveries that ParB proteins bind to and hydrolyze CTP [19, 37, 40] established models involving ParB sliding on DNA [19, 21]. Here, a ParB dimer adopts an open NTD conformation (the NTD-gate) and binds to the *parS* DNA sequence through the helix-turn-helix motif on the CDBD (the DNA-gate). CTP binding self-dimerizes the NTD-gate, closing the DNA-gate and forming a DNA sliding clamp [20, 21, 37, 40]. The NTD- and DNA-gate closures release *parS* DNA into a compartment between the DNA-gate and CTD, allowing ParB to slide away from *parS* [41, 42]. CTP hydrolysis reopens the gates, causing ParB to be unloaded and recycled [20, 21, 40].

In *B. subtilis*, the CTD contains a region with five lysines (K252, K255, K256, K257, and K259). Mutating a subset of them (K255A–K257A or K252A–K255A–K259A) diminished DNA condensation in a magnetic tweezer-based assay [33]. The results indicate that the positively charged lysine residues directly interact with the negatively charged DNA backbone. Thus, it is puzzling how the ParB clamp slides while its CTD interacts with DNA. The understanding of ParB CTD dynamics and their effects on CTD functions is limited. In this study, we employed NMR, single-molecule experiments, biochemical approaches, molecular dynamics (MD) simulation, cellular fluorescence imaging, and sporulation initiation assay to investigate the molecular mechanisms and cellular function of CTD dynamics. We demonstrate that each CTD lysine has a distinct role. Fast lysine dynamics, occurring on timescales of picoseconds to nanoseconds, promote efficient DNA sliding. We also show that any single lysine mutation substantially impacts DNA bridging *in vitro* and argue that the integrity of these five lysines is crucial for positioning DNA properly within the ParB sliding clamp. Our data show that CTD dimerization is important for ParB foci formation and sporulation initiation. Additionally, we provide insights into how DNA-binding proteins across diverse protein families use multiple basic residues for fast dynamics.

Materials and methods

Plasmids and DNA preparation

The plasmids with the coding sequence of His6-SUMO-tagged *B. subtilis* ParB (BsParB) proteins were constructed by assembling double-stranded gBlocks^{TM} gene fragments. Briefly, a polymerase chain reaction (PCR) was performed with the plasmid that encodes His6-SUMO-BsParB [wild-type (WT)] (m0041 = pTG011) to generate a linearized vector devoid of a part of the SUMO-tag coding sequence and the entire WT BsParB. Double-stranded gBlocks^{TM} gene fragments in which sequences encode for the full-length or the CTD of BsParB proteins were commercially synthesized (Integrated DNA Technologies, Coralville, IA). The desired plasmids were generated from the linearized vector and synthesized inserts by following the NEBuilder HiFi DNA Assembly Master Mix (New England Biolabs, E2621S, Ipswich, MA) protocol. The reaction mixtures were used to transform NEB 5-alpha competent *Escherichia coli* cells. After performing minipreps, Sanger (Psomagen, Rockville, MD) or whole plasmid sequencing (Plasmidsaurus, Louisville, KY) was used to confirm the sequences of the plasmids.

Ten-basepair DNA hairpins (GCGTACATCATTCCCTGATGTACGC) for NMR relaxation studies were prepared as previously reported by Fisher *et al.* [33] and concentrated in phosphate-buffered saline (PBS) buffer (1.8 mM KH_2PO_4, 10 mM NaH_2PO_4, 137 mM NaCl, and 2.7 mM KCl, pH 6.1).

Culture growth and *B. subtilis* ParB C-terminal domain purifications for NMR study

Each plasmid encoding His6-SUMO-BsParB(217–282; CTD) construct (m0083, m0134, m0137, and m0139 for WT, K256A, K259A, and K252A–K255A–K259A, respectively) was transformed into BL21(DE3)pLysS *E. coli* competent cells. Three milliliters of Luria-Bertani (LB) broth was inoculated with the transformed cells from a single colony in the presence of 100 μg ml^{-1} ampicillin and 20 μg ml^{-1} of chloramphenicol. After growing the cells for 5–6 h at 37°C in a shaking incubator (250 rpm), 0.8 ml of the cell culture was transferred into 40 ml of 90:10 (vol/vol) M9 minimal/LB media that contains U-^{15}N NH_4Cl and incubated overnight at 37°C. The next morning, 20 ml of the overnight culture was transferred into 1 l of M9 minimal media and allowed to grow at 37°C while shaking at 250 rpm. Once the OD_{600} reached 0.6–0.8, protein overexpression was induced by adding isopropyl β-D-1-thiogalactopyranoside (IPTG; 0.5 mM final

concentration). After induction by IPTG, the cell culture was allowed to grow at 37°C for 4 h. Cells were harvested by centrifugation. The cell pellets were resuspended in lysis buffer (20 mM Tris, pH 8.0, 1 M NaCl, 20 mM imidazole) containing a Complete Mini-ethylenediaminetetraacetic acid (EDTA)-free protease inhibitor cocktail (Roche, 04693159001, Basel, Switzerland) and 0.1 mM phenylmethylsulfonyl fluoride (PMSF) and then flash-frozen.

After thawing the cells, we added additional PMSF to 1.0 mM final concentration, 0.25 mg ml^{-1} lysozyme, 750 U universal nuclease (Thermo Fisher Scientific, 88701, Waltham, MA), and 5.0 mM 2-mercaptoethanol (βME). After 30 min on ice, cells were sonicated with a microtip (amplitude 40%, total time 15 min, pulse on: 4.0 s, pulse off: 2.0 s) on Branson sonifier (Emerson, SFX150, St. Louis, MO). The cell lysate was first centrifuged at 11 000 × *g* with an FA-6×50 rotor in a centrifuge (Eppendorf, 5910R, Hamburg, Germany) for 30 min at 4°C. The supernatant was once again centrifuged at 20 133 × *g* for 30 min. The supernatant containing His6-SUMO-BsParB(217–282) was collected and mixed with 6 ml of Ni-NTA agarose solution (Qiagen 30230, Hilden, Germany) for a 3 ml bed volume and supplemented with one tablet of Complete Mini-EDTA-free protease inhibitor cocktail. The supernatant was incubated for 1 h. After applying the mixture of supernatant and Ni-NTA resin, we washed the column with 30 ml of lysis buffer supplemented with 5 mM $MgCl_2$ and 5 mM βME. Then, we washed the column with salt reduction buffer (20 mM Tris, pH 8.0, 350 mM NaCl, 20 mM imidazole, 5 mM $MgCl_2$, 5 mM βME). Finally, proteins were eluted with elution buffer (20 mM Tris, pH 8.0, 350 mM NaCl, 250 mM imidazole, 5 mM $MgCl_2$, 5 mM βME). After each step, we collected fractions and analyzed them using a sodium dodecyl sulfate–polyacrylamide gel electrophoresis (SDS–PAGE). Fractions with identified His-SUMO-BsParB(217–282) were combined, supplemented with SUMO cleaving His-tagged Ulp1 protein, and left to incubate for 1 h at 4°C. After 1 h, the protein solution was transferred into a dialysis tube. We dialyzed the protein three times (1 h in 500 ml, overnight in 1 l, and 2.5 h in 500 ml) against ParB dialysis/storage 1 buffer (20 mM Tris, pH 8.0, 350 mM NaCl, 10 mM imidazole, 5 mM βME, 1 mM $MgCl_2$, 10% glycerol). Collected from the dialysis bag, the protein solution was remixed with the Ni-NTA resin and incubated for 1 h. The mixture was added to a 5 ml polypropylene column (Qiagen, 34964, Germantown, MD), and the unbound CTD (devoid of His-SUMO) protein [BsParB(217–282)] was eluted. ParB dialysis/storage 2 buffer (20 mM Tris, pH 8.0, 350 mM NaCl, 10% glycerol) was used to elute more unbound CTD. The collected fractions were analyzed with an SDS–PAGE gel. Pure CTD fractions were consolidated. The final protein was snap-frozen in liquid nitrogen and stored at −80°C. CTD concentration was determined by UV-Vis using theoretical extinction coefficients of 2560 M^{-1} cm^{-1}.

Overexpression and purification of full-length *B. subtilis* ParB proteins

Full-length ParB proteins were overexpressed and purified based on the overexpression and purification protocols for His6-SUMO-BsParB(217–282) protein and those from our previous work [43], except for the following modifications: (i) Rosetta2(DE3)pLysS cells were transformed, and only LB medium was used in culturing the transformed cells. (ii) IPTG was added when the OD_{600} reached 0.4–0.5. (iii) After adding IPTG, the culture was grown for 4 h at 30°C. (iv) the sonication was done at 30% amplitude, for a total of 10 s with 1 s pulses on and 1 s pulses off. (v) Apyrase was supplemented into the clarified supernatant to deplete cellular nucleoside triphosphates. (vi) For the protein concentration determination, 7450 M^{-1} cm^{-1} was used as the theoretical extinction coefficient. (vii) Purified proteins were dialyzed against ParB dialysis/storage 2 buffer.

NMR sample preparations

Uniformly ^{15}N-labeled samples for solution NMR measurements were prepared from purified protein by buffer exchange in PBS (pH 6.1), with 10% D_2O and 200 mM 4,4-dimethyl-4-silapentane-1-sulfonic acid (DSS). NMR samples were prepared with different protein concentrations and loaded into 1.3 mm NMR tubes. DNA-bound protein samples were prepared by adding the 10-base pair hairpin DNA in 0.25–1.25 equivalents.

NMR datasets for ^{1}H-^{15}N HSQC (heteronuclear single quantum coherence) [44], ^{1}H-^{15}N T_1 [45, 46], and heteronuclear NOE (nuclear Overhauser effect) bi-dimensional experiments [47] were collected at 308 K, utilizing NMR 500 MHz spectrometer (Bruker, Billerica, MA). NMR data sets for T_2 [46] were collected at 308 K utilizing both NMR 500 and NMR 700 spectrometers (Bruker, Billerica, MA). NMR data sets for $T_1\rho$ [48, 49] were collected at 308 K utilizing the NMR 700 MHz spectrometer.

^{15}N relaxation experiments

We used the two-dimensional ^{1}H-^{15}N HSQC pulse sequence "hsqct1etf3gpsi3d" to measure heteroatom T_1 relaxation time [50, 51]. Pseudo three-dimensional ^{1}H-^{15}N HSQC spectra for longitudinal relaxation time T_1 of CTD were acquired in Q.F. mode for proton dimension (F1) and Echo-Antiecho mode for nitrogen dimension (F2). The spectral widths were 16 ppm for direct and 35 ppm for indirect dimensions, respectively. Proton and nitrogen carrier frequencies were centered at 4.703 and 117 ppm, respectively. The time points collected were 2048 for the proton dimension and 256 for the nitrogen dimension. The acquisition time was 0.000564 s for proton and 0.0722 s for nitrogen. The number of scans acquired was 32. ^{15}N T_1 values were measured from the spectra and recorded with seven different durations of the delay T: $T = 0.01$, 0.08, 0.2, 0.4, 0.6, 0.8, and 1.0 s. The measurements were repeated three times for a delay of 0.2 s.

We used the two-dimensional ^{1}H-^{15}N HSQC pulse sequence "hsqct2etf3gpsi3d" to measure heteroatom T_2 relaxation time [52]. Pseudo three-dimensional ^{1}H-^{15}N HSQC spectra for transverse relaxation time T_2 of CTD were acquired in Q.F. mode for proton dimension (F1) and in Echo-Antiecho mode for nitrogen dimension (F2). Proton and nitrogen carrier frequencies were centered at 4.703 and 117 ppm, respectively. The spectral widths were 16 ppm for direct and 35 ppm for indirect dimensions. The time points collected were 2048 for the proton dimension and 256 for the nitrogen dimension. The acquisition time was 0.000689 s for the proton dimension and 0.0722 s for the nitrogen dimension. The number of scans acquired was 32. ^{15}N T_2 values were measured from the spectra recorded with nine different durations of the delay T: $T = 0$, 0.016, 0.032, 0.048, 0.064, 0.080,

0.096, 0.112, and 0.128 s. The measurements were repeated three times for a delay of 0.032 s.

For the heteronuclear NOE pulse sequence "hsqcnoef3gpsi3d" [53], spectra were recorded in the presence and absence of ^{1}H saturation: 4 s saturation plus 1 s recycle delay, and the reference experiment with 5 s recycle delay. Heteronuclear ^{15}N-^{1}H NOE spectra for CTD were acquired in Q.F. (no frequency) mode for the proton dimension (F1) and in Echo-Antiecho mode for the nitrogen dimension (F2). Proton and nitrogen carrier frequencies were centered at 4.703 and 117 ppm, respectively. The spectral widths were 16 ppm for direct and 35 ppm for indirect dimensions. The time points collected were 2048 for the proton dimension and 512 for the nitrogen dimension. The acquisition time was 0.0002 s for the proton dimension and 0.144 s for the nitrogen dimension. The number of scans acquired was 32. The experiment was recorded for 1 day and 15 h.

We used the two-dimensional ^{1}H-^{15}N HSQC pulse sequence "hsqctretf3gpsi3d" to measure heteroatom $T_1\rho$ relaxation time [48, 49]. Pseudo three-dimensional ^{1}H-^{15}N HSQC spectra for relaxation time $T_1\rho$ of CTD were acquired in Q.F. mode for proton dimension (F1) and Echo-Antiecho mode for nitrogen dimension (F2). The spectral widths were 16 ppm for direct and 35 ppm for indirect dimensions, respectively. Proton and nitrogen carrier frequencies were centered at 4.703 and 117 ppm, respectively. The time points collected were 2048 for the proton dimension and 256 for the nitrogen dimension. The acquisition time was 0.0515499 s for proton and 0.0901120 s for nitrogen. The number of scans acquired was 16. ^{15}N $T_1\rho$ values were measured from the spectra and recorded with five different durations of the delay T: T = 0.002, 0.008, 0.032, 0.064, 0.080 s. The measurements at 0.032 s delay were repeated three times.

NMR data processing

All obtained NMR spectra were processed with NMRpipe [54] and analyzed with Sparky (version 3.113. The University of California, San Francisco). A forward linear prediction to twice the number of original data points, followed by zero filling to twice the total number of points, was used for all experiments prior to the Fourier transformation. 45°-shifted sine bell apodization with a water suppression function was used for both dimensions.

Determination of R_1, R_2, $R_1\rho$, R_{ex}, NOE, and error analyses

To determine R_1, R_2, and $R_1\rho$, the T_1, T_2, and $T_1\rho$ relaxation data obtained by NMR relaxation experiments were analyzed with the routine available within SPARKY. We measured the intensities of the ^{15}N-^{1}H cross-peaks from the relaxation experiments for the various recovery delay times using SPARKY software. The peak intensities for the protein residues were then fitted to the exponential decay equation (1) by the SPARKY routine to determine T_1, T_2, and $T_1\rho$, where T_1, T_2, and $T_1\rho$ are the relaxation rates. Knowing T_1, T_2, and $T_1\rho$, we calculated R_1, R_2, and $R_1\rho$ as $R_1 = 1/T_1$, $R_2 = 1/T_2$, and $R_1\rho = 1/T_1\rho$.

$$I(t) = A + Be^{-\frac{t}{T_{1,2}}}. \quad (1)$$

The experimental R_{ex} parameters for the individual residues were calculated by subtracting $R_1\rho$ from R_2, both determined at 16.4 T field (700 MHz).

The {^{1}H}-^{15}N heteronuclear NOEs were calculated from the ratio of cross-peak intensities in the two experiments: with and without proton saturation (equation (2)).

$$\mathrm{NOE} = \frac{I_{sat}}{I_{non-sat}}. \quad (2)$$

The errors for R_1, R_2, and $R_1\rho$ were calculated from estimated T_1, T_2, and $T_1\rho$ errors from the fitting routine. We estimated uncertainty in per-residue R_1, R_2, and $R_1\rho$ by combining two components: the within-fit standard error from fits of the relaxation curves, and a between-fit variability obtained from three independent global fits that differed only in which of the replicated spectra at a single delay time (0.2 s for R_1 and 0.032 s for R_2 and $R_1\rho$) was used. NOE errors were calculated from the RMS noise errors in each spectrum.

Modelfree calculations

r2r1_tm and quadric_diffusion routines developed by the Palmer group [55] were used to determine the initial value for overall correlation time (τ_m) and the initial estimate of the diffusion tensor. The latter was a prerequisite to determine the appropriate motional model (spherical, axially symmetric, or fully anisotropic). r2r1 routine calculates R_2/R_1 ratio of the individual residues ^{15}N amide peaks. The R_2/R_1 ratio can estimate the overall molecular tumbling correlation time, τ_m. This estimation is achieved when conformational exchanging motions are absent and internal motions are fast, allowing the R_2/R_1 ratio to depend only on the overall rotational correlation time (τ_m) [50, 56]. Therefore, for our τ_m calculations, we excluded residues with low NOE that correspond to a large amplitude of internal motions and are indicative of a timescale of motions longer than hundreds of picoseconds [57]. Residues having a greater than 1.0 standard deviation (SD) for the R_2/R_1 ratio were also excluded from the calculations due to the possible effect of the additional contribution of conformational exchange R_{ex} to R_2 [50, 58]. The calculated τ_m values are then fed into the quadric_diffusion routine. To calculate the initial estimate of the diffusion tensor, along with the τ_m values, we used the PDB file of the NMR structure of apo CTD (PDB entry 5NOC) modified by the "pdbinertia" program [55].

To select the dynamic model describing the residues' internal motion, we used the FAST-ModelFree program developed by Loria and Cole [59]. This program performs model-free calculations based on model-free formalism developed by Lipari and Szabo [60]. The model-free formalism allows the data from relaxation experiments (R_1, R_2, NOE) to be analyzed by fitting several "model-free" spectral density functions (Supplementary Table S1). Through these calculations, we can obtain two essential parameters: S^2 and τ. S^2 is an order parameter reflecting the rigidity of the vector, N–H bond in the case of protein, with τ being a timescale of the vector's internal motion. The FAST-Modelfree conducts the model calculation through the Modelfree program written by the Palmer group [61–63], which fits a model function for each residue. Our input file for the FAST-Modelfree program had an N–H bond length set to 1.02 Å and ^{15}N chemical shift anisotropy equal to 172 ppm.

Chemical shift perturbation analysis

The following equation (3) calculates chemical shift perturbations (CSPs) for backbone amides between initial and final

states 1 and 2 [63].

$$\mathrm{CSP} = \sqrt{[(\delta_{H2} - \delta_{H1})^2 + \alpha * (\delta_{N2} - \delta_{N1})^2]}. \quad (3)$$

$\delta_{H1,2}$ and $\delta_{N1,2}$ values are the ^{1}H and ^{15}N chemical shifts for states 1 and 2, respectively, with $\alpha = 0.2$.

DNA substrate preparation for single-molecule experiments

Unmodified bacteriophage λ-DNA was purchased (New England Biolabs, N3013S, Ipswich, MA). The engineered λ-DNA harboring one *parS* site in the middle (1-*parS* DNA) was prepared from the λ^{parS} lysogen strain [38]. Cells were grown in 250 ml of LB at 30°C in a 2.8-l flask. When the OD_{550} reached 0.4, 250 ml 50°C LB was added to the flask. At the same time, the flask was shifted to a 40°C water shaker. This allowed the culture to quickly shift to 40°C. After an additional 2.5 h of shaking at 40°C, the culture was rapidly cooled down by swirling the flask in ice water. The culture was centrifugated at 5000 × *g*. The supernatant was discarded, and the cell pellet was resuspended in 1 ml of lambda-dil buffer (10 mM Tris, pH 7.4, 5 mM $MgSO_4$, 0.01% gelatin) and snap-frozen in liquid nitrogen. The cells were thawed at room temperature and left at 30°C for 30 min to allow lysis. 10 μg ml^{-1} of DNase I and 10 μg ml^{-1} of RNase I were added and incubated at 37°C for 1 h. After adding 5 ml of lambda-dil(minus gelatin) buffer (10 mM Tris, pH 7.4, 5 mM $MgSO_4$) and 6 ml of the saturated CsCl, cells were spun at 31 000 rpm (∼164 450 × *g*) for over 40 h (Thermo Fisher Scientific, Sorvall WX80+, Waltham, MA). The phage particles were withdrawn using a syringe and dialyzed against lambda-dil(minus gelatin) buffer. Subsequently, 100 μg ml^{-1} of proteinase K and 0.5% of SDS were supplemented and incubated at 56°C for 1 h. The 1-*parS* DNA was obtained by DNA extraction procedures using phenol/chloroform/isoamyl alcohol (25:24:1) followed by chloroform, and dialyzed against a storage buffer (50 mM Tris, pH 7.5, 10 mM $MgCl_2$.)

The overhangs of bacteriophage lambda DNA (or 1-*parS* DNA) were employed to tag one end with biotin and the other end with digoxigenin, as outlined in our previous works [64]. This allows lambda DNA tethering to the microfluidic flow cell surface through neutravidin-biotin interactions facilitated by biotin. The opposite end of lambda DNA was labeled with digoxigenin, essential for attaching anti-digoxigenin antibody-conjugated quantum dot 605 (Invitrogen Q21501MP, Waltham, MA). Briefly, a biotinylated oligo was annealed to a complementary overhang, followed by ligation, and a similar process was carried out for digoxigenin oligo. The removal of excess short oligos was executed through electrophoresis, and DNA substrates were obtained via ethanol precipitation.

Microfluidic flow cell preparation

Cover glasses were effectively surface-passivated using (3-aminopropyl)triethoxysilane (Millipore Sigma, A3648, St. Louis, MO) followed by a mixture of polyethylene glycol (PEG) and its biotinylated version (Laysan Bio, MPEG-SVA-5000-1GR and Biotin-PEG-SVA-5000-100MG, Arab, AL), as stated in previous publications [64]. A microfluidic flow cell was constructed by drilling parallel holes on a quartz plate (Technical Glass Product, Paineville, OH) and placing double-sided tape (Grace Bio-Labs, SA-S-1L, Bend, OR) between a PEGylated cover glass and the modified quartz plate. The parallel-affixed double-sided tapes create a rectangular cell channel with a defined height and width. The inlet tube (7 cm) and outlet tube (2.5 cm) were inserted through holes in the quartz plate and sealed airtight with epoxy. The PE60 inlet tube at one channel end was immersed in a buffer-containing tube, while the outlet tube at the other end was connected to a syringe on a syringe pump (Harvard Apparatus, 70-4504, Holliston, MA).

Single-molecule DNA flow-stretching and data analysis

Approximately 4% of the PEG on the surface-passivated cover glass contains biotins, acting as a neutravidin-binding platform. 0.25 mg ml^{-1} of neutravidin was administered, followed by quantum dot-labeled biotinylated lambda DNAs. The removal of unlabeled quantum dots and untethered DNAs was achieved by washing the flow cell with an imaging buffer (10 mM Tris, pH 7.5, 100 mM NaCl, and 2.5 mM $MgCl_2$). Movie acquisition was acquired after a minimum of 2 min without buffer flow to ensure that the average quantum dot position coincides with the DNA tether point due to the lack of flow. Subsequently, DNAs were stretched by initiating the flow of protein in imaging buffer (50 ml min^{-1}). Experiments were conducted using a total internal reflection fluorescence microscope (Olympus, IX-83, Waltham, MA) with a 532 nm laser (Coherent, Santa Clara, CA). Recorded images were acquired with the Micro-Manager software [65], and DNAs' regions of interest were set using FIJI software [66]. Custom MATLAB software codes, based on Gaussian fitting, were utilized to determine quantum dot positions. Detailed procedures and the custom MATLAB codes are accessible in our prior publications [64, 67]. The DNA compaction rates were compared via nonparametric Mann–Whitney test using Prism software (GraphPad, San Diego, CA).

Size exclusion chromatography with multi-angle light scattering

WT ParB and its mutant variants at 0.65 mg ml^{-1} (20 mM), and bovine serum albumin (BSA) standard at 2.0 mg ml^{-1} were run at a flow rate of 0.2 ml min^{-1} in running buffer (20 mM Tris, pH 8.0, 350 mM NaCl) on a Cytiva Superdex 200 Increase 200 10/300 GL size-exclusion chromatography column. The column was attached to an AKTA Pure fast protein liquid chromatography system coupled with a Wyatt Dawn multi-angle light scattering detector (Wyatt Technology, Goleta, CA) and a Wyatt Optilab differential refractive index detector. Chromatograms were analyzed using the ASTRA 8 software (Wyatt Technology, Goleta, CA) to determine the molecular weights and oligomeric states.

Molecular dynamics simulations

MD simulations were performed with GROMACS software (version 24.2) [68]. The atomistic model of apo CTD was constructed on the available NMR structure (PDB: 5NOC), while the DNA-bound CTD model was constructed using the AlphaFold server [69]. The protein was inserted in a cubic box with a buffer width of 1.5 nm. We solvated the CTD with explicit water, along with neutralization by chlorine and sodium ions to 0.15 M concentration. To describe proteins, DNA, and ions, we used the AMBER99SB force field [70]. The TIP3P model [71] was used to treat the water environ-

ment. The energy minimization step was performed with the steepest descent algorithm until the maximum force fell below 1000 kJ mol^{-1} min^{-1}. Coulomb interactions, van der Waals interactions, and neighbor list cut-off distance were 1.0 nm. We applied the Verlet cut-off scheme for the neighbor list with the electrostatic interactions calculated by the particle mesh Ewald [72] method with a grid spacing of 0.125 nm. The system was first equilibrated with a position restraint on all protein-heavy atoms to hold a temperature at 308 K with the use of the v-rescale thermostat [73] and then brought to 1 bar pressure with the use of an improved version of the Berendsen barostat (c-rescale) [74]. All bonds to hydrogens were constrained with the LINKS algorithm [75]. Following the equilibration stage, our 500 ns production run had position restraints removed.

We used the truncated average approximation [76] to the Lipari–Szabo model-free approach [60] to calculate the order parameters (S^2). The S^2 was determined by taking the average over the second half of each C(t) relaxation curve, where C(t) is the angular autocorrelation function of the second-order Legendre polynomial for the unit vector pointing along the amide bond vector calculated from trajectories generated during the production runs. Average structures were obtained over the duration of the simulation.

Electrophoretic mobility shift assay

The 100 nM stock of 169-base pair double-stranded DNA (dsDNA) gBlocks™ fragment devoid of any *parS* sites (Integrated DNA Technologies, Coralville, IA) and the 10 μM BsParB protein stocks were prepared in ParB100WM buffer (10 mM Tris, pH 7.5, 100 mM NaCl). The DNA substrate (final concentration: 8 nM) and desired concentrations of the proteins were incubated for 30 min on ice, where 1/5 volume of the reaction mixture was the 5× sample buffer (50 mM Tris–HCl, pH 8.0, 5 mM EDTA, 25% glycerol, 0.2% bromophenol blue, 0.2% xylene cyanole FF). During DNA–protein incubation, a 5% TBE (tris-borate-EDTA) precast gel (Bio-Rad, 4565015, Hercules, CA) in TBE buffer (89 mM Tris, pH 7.6, 89 mM boric acid, 2 mM EDTA) was pre-run at 120 V at 4°C for 30 min to remove ions from the gel. Upon completion of the pre-run, 17 μl of the protein–DNA mixture were loaded onto each gel well, and an electrophoresis was performed at 120 V at 4°C for 1 h. The gel was stained for 30 min in GelRed (Biotium, 41003, Fremont, CA) solution before imaging.

Plasmid construction for *in vivo* experiments

The following variants of **pWX563** [*pelB::Psoj-mgfpmut3-spo0J (ΔparS) tet*] [38] were constructed through the isothermal assembly of two DNA fragments amplified from pWX563 using primers specified in Supplementary Table S2. All the constructs were sequenced by whole plasmid sequencing. Detailed information on the plasmids is available in Supplementary Table S2.

pWX1227 [*pelB::Psoj-mgfpmut3-spo0J-A232G(ΔparS) tet*] used oWX3485 and oWX418 for fragment 1 and oWX3484 and oWX2071 for fragment 2.

pWX1228 [*pelB::Psoj-mgfpmut3-spo0J-E261A(ΔparS) tet*] used oWX3487 and oWX418 for fragment 1 and oWX3486 and oWX2071 for fragment 2.

pWX1229 [*pelB::Psoj-mgfpmut3-spo0J-K257A(ΔparS) tet*] used oWX3489 and oWX418 for fragment 1 and and oWX3488 and oWX2071 for fragment 2.

pWX1230 [*pelB::Psoj-mgfpmut3-spo0J-K256A(ΔparS) tet*] used oWX3491 and oWX418 for fragment 1 and oWX3490 and oWX2071 for fragment 2.

pWX1323 [*pelB::Psoj-mgfpmut3-spo0J-K252A (ΔparS) tet*] used oWX3807 and oWX418 for fragment 1 and oWX3806 and oWX2071 for fragment 2.

pWX1324 [*pelB::Psoj-mgfpmut3-spo0J-K259A (ΔparS) tet*] used oWX3809 and oWX418 for fragment 1 and oWX3808 and oWX2071 for fragment 2.

pWX1325 [*pelB::Psoj-mgfpmut3-spo0J-K252A-K259A (ΔparS) tet*] used oWX3811 and oWX418 for fragment 1 and oWX3810 and oWX2071 for fragment 2.

pWX1326 [*pelB::Psoj-mgfpmut3-spo0J-K252A-K255A-K259A (ΔparS) tet*] used oWX3813 and oWX418 for fragment 1 and oWX3812 and oWX2071 for fragment 2.

pWX1399 [*pelB::Psoj-mgfpmut3-spo0J-K255A (ΔparS) tet*] used oWX4066 and oWX418 for fragment 1 and oWX4067 and oWX2071 for fragment 2.

Strain building

Bacillus subtilis strains (Supplementary Table S3) were derived from the PY79 WT strain. Strains were built through transformations of plasmids or gDNA (genomic DNA). After transformation into *B. subtilis*, gDNA was extracted and the mutated region was amplified using oML85 and oWX507. The amplicon was sequenced by whole plasmid sequencing (linear/amplicon). Strains were grown in defined rich casein hydrolysate (CH) medium at 37°C with aeration [77].

Fluorescence microscopy

Fluorescence microscopy was performed according to a previously described procedure [78] . Specifically, cells were grown in defined rich CH medium [77] at 37°C to the exponential phase (OD_{600} between 0.2 and 0.5). Cells were immobilized using 2% agarose pads containing growth media. Fluorescence microscopy was performed on a Ti2E microscope (Nikon, Melville, NY) equipped with a Plan Apo 100×/1.4NA phase contrast oil objective and an sCMOS (scientific complementary metal-oxide-semiconductor) camera. The exposure times for phase contrast, GFP, and mCherry were 500 ms, 1 s, and 300 ms, respectively. Images were cropped and adjusted using NIS-Elements Advanced Research Imaging Software. The fluorescence of different strains was scaled the same for comparison. Fluorescence intensities were quantified using MetaMorph software (Molecular Devices, San Jose, CA). Figures were prepared in Adobe Illustrator.

Heat resistance sporulation assay

Sporulation efficiency was determined as described by Harwood and Cutting [77]. Briefly, a freshly streaked colony was inoculated in 2 ml of Difco Sporulation Medium (DSM) and incubated for 24 h in a roller drum at 37°C. The cultures were serially diluted by 10-fold in the dilution medium containing T-Base and 1 mM $MgSO_4$. To determine total colony-forming units, 200 μl of the 10^{-6} dilution and 50 μl of the 10^{-5} dilution were plated on separate DSM agar plates. To kill the non-sporulated cells, the diluted cultures were incubated at 80°C for 20 min. One hundred microliters of the heat-killed

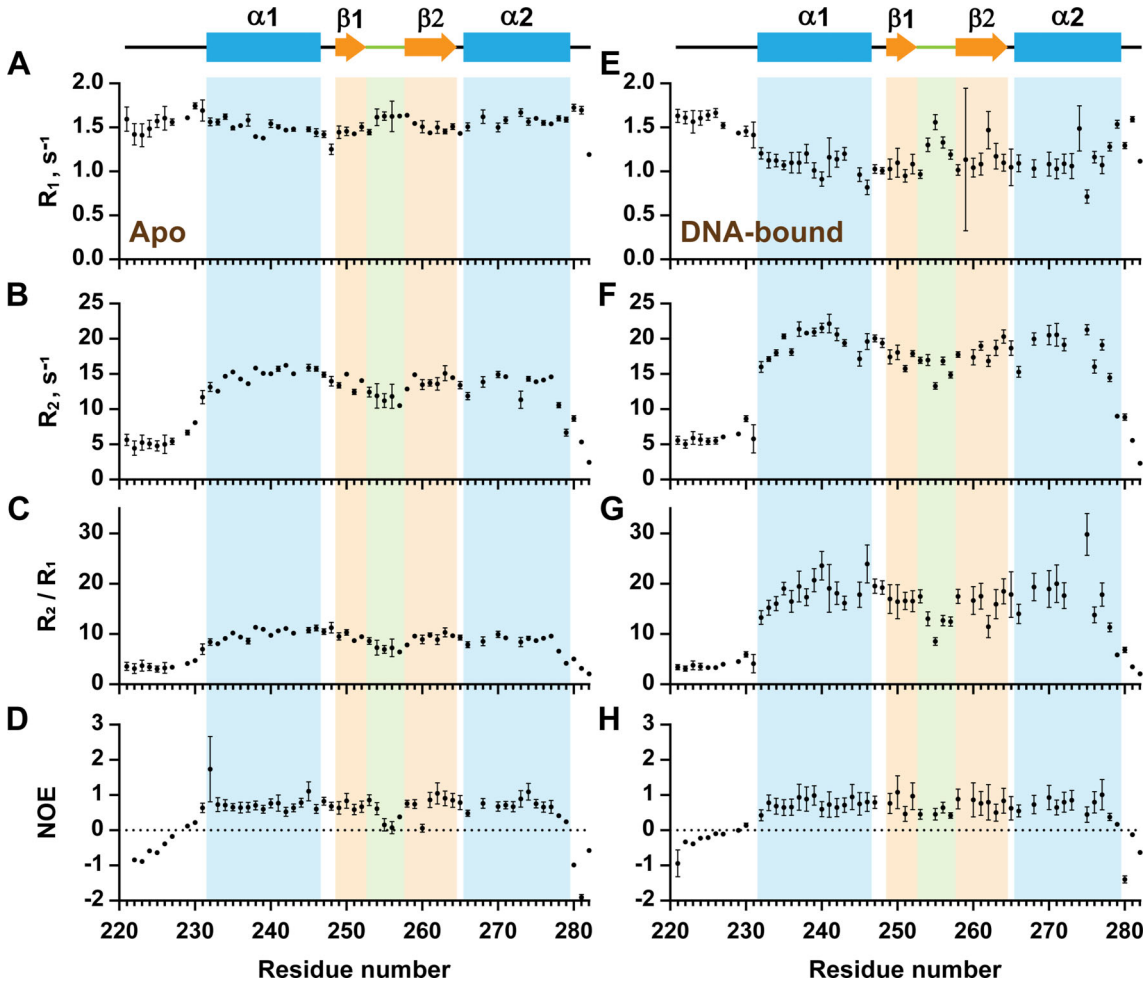

Figure 1. Relaxation data of apo and DNA-bound CTD at 11.7 T. Four hundred micromolar CTD in PBS buffer, pH 6.1 at 308 K. For apo CTD: (**A**) R_1, (**B**) R_2, (**C**) R_2/R_1, and (**D**) NOE. For DNA-bound CTD: (**E**) R_1, (**F**) R_2, (**G**) R_2/R_1, and (**H**) NOE. The secondary structure of the apo CTD determined from the NMR structure (PDB: 5NOC) is displayed at the top: α-helices (cyan bars), β-strands (light orange arrows), loops (black lines), and linker region (light green). Error bars: SD.

dilutions were plated onto DSM agar plates. All plates were incubated overnight at 37°C.

Results

NMR parameters (^{15}N R_1, R_2, and NOE) of apo CTD indicate fast backbone dynamics in the lysine residues

The mobility of the protein backbone chain is important for its function. For the *B. subtilis* ParB (BsParB) protein, the CTD is a nonspecific DNA-binding domain [33], and we hypothesize that its backbone dynamics promote DNA sliding. To understand the CTD backbone dynamics upon nonspecific DNA binding, we performed NMR relaxation studies for ParB CTD(217–282) expressed in *E. coli* (Supplementary Fig. S1C and D). As a starting point, building upon previously reported residue assignments of apo-CTD [33], we analyzed 57 non-overlapping peaks. These assignments are presented on a ^{1}H-^{15}N HSQC spectrum of CTD at 308 K, pH 6.1 (Supplementary Fig. S2A).

Following the residue assignments, to study the protein motion of apo CTD for each backbone amide on a fast (picoseconds to nanoseconds) time scale, we characterized three relaxation parameters: the self-relaxation rates (^{15}N R_1 and R_2) and the steady-state heteronuclear Overhauser effect ($\{^{1}H\}^{15}N$–NOE) that corresponds to dipolar cross-relaxation between two coupled ^{1}H and ^{15}N spins (Fig. 1A–D and Table 1). The initial mean correlation time (τ_m) was 11.02 ± 0.66 (mean ± SD) ns, and the mean R_2/R_1 ratio equals 7.92 ± 2.65 (SD). (see "Materials and methods" section). R_2/R_1 for the apo CTD shows different dynamics between secondary structures along the backbone. Secondary structures on the N-terminal half of the CTD have higher than average R_2/R_1 (9.079), suggesting intermediate-timescale motion. On average, the N-terminal half exhibits larger R_2/R_1 values compared to the secondary structures of the C-terminal half of the CTD (Fig. 1C). The low average R_2/R_1 values of the C-terminal α-helix and especially the linker with its DNA binding lysine residues suggest mostly fast timescale backbone dynamics of these regions in the apo CTD (Fig. 1C). The apo relaxation data indicate distinct dynamics between different secondary structures and reveal highly dynamic linker regions.

Determining apo CTD's dynamic parameters (S^2, R_{ex}, τ) with Model-Free analysis

R_2/R_1 data, and those from pdbinertia (see "Materials and methods" section), were further used to estimate rotational diffusion tensors (for overall tumbling motion) and to de-

Table 1. Average relaxation parameters per secondary structures and terminal loops (top half) and average order parameters, S^2 per secondary structures, and terminal loops (bottom half) in apo and DNA-bound CTD.

	N-Term (221–230)	α-helix 1 (231–246)	Loop 1 (247–248)	β-strand 1 (249–252)	Linker (253–257)	β-strand 2 (258–264)	Loop 2 (265)	α-helix 2 (266–279)	C-term (280–282)
Apo CTD									
R_1	1.556	1.516	1.337	1.459	1.589	1.514	1.433	1.576	1.538
R_2	5.610	14.664	14.441	13.725	11.578	14.027	13.414	12.805	5.499
R_2/R_1	3.612	9.781	10.870	9.501	7.307	9.278	9.301	8.301	3.518
NOE	−0.396	0.702	0.755	0.682	0.416	0.746	0.786	0.669	-1.159
DNA-bound CTD									
R_1	1.570	1.103	1.018	1.040	1.270	1.146	1.047	1.137	1.335
R_2	6.038	18.607	19.731	17.291	15.789	18.332	18.688	15.928	5.584
R_2/R_1	3.880	17.355	19.388	16.628	12.845	16.261	17.853	16.855	4.142
NOE	−0.240	0.746	0.777	0.818	0.587	0.724	0.624	0.664	-0.717
	N-Term (229–230)	α-helix 1 (231–246)	Loop 1 (247–248)	β-strand 1 (249–252)	Linker (253–257)	β-strand 2 (258–264)	Loop 2 (265)	α-helix 2 (266–279)	C-term (280–282)
Apo CTD									
S^2	0.46	0.91	0.87	0.89	0.77	0.90	0.87	0.84	0.13
S^2 err	0.03	0.02	0.02	0.02	0.04	0.02	0.01	0.02	0.03
DNA-bound CTD									
S^2	0.31	0.85	0.89	0.84	0.77	0.88	0.90	0.75	0.21
S^2 err	0.02	0.03	0.02	0.03	0.02	0.03	0.05	0.04	0.01

termine the appropriate motional model (spherical, axially symmetric, or fully anisotropic). The results of the quadric_diffusion program (see "Materials and methods" section) were collected in Supplementary Table S4. The model of molecular tumbling was selected with the smallest chi-square (χ^2) and an F value. For the apo CTD, the overall tumbling is fully anisotropic with anisotropy $D_A = 2D_{zz}/(D_{xx} + D_{yy})$ equal to 1.282 ± 0.043 (SD) based on comparing χ^2 and F statistics for each model. The average overall rotational correlation time, τ_m, equals $(6\times D_{iso})^{-1} = 11.08 \pm 0.06$ (SD) ns. We should note that the degree of anisotropy is small, so we can treat the tumbling of apo CTD as axially symmetric with the FAST-Modelfree program applying output pdb file for anisotropic diffusion analysis. We applied initial estimates of τ_m, D_{par}/D_{per}, θ and φ, and other relaxation parameters in the FAST-Modelfree program (See "Materials and methods" section) using the axially symmetric model for rotational diffusion tensor. The program then iteratively refined parameters such as S^2 (order parameter) and τ_e to fit ^{15}N relaxation data. Five spectral density functional models fit the data (Supplementary Table S1). The results for rotational diffusion tensor show that the relaxation of NH vectors for the majority of the apo CTD residues fit the simplest model, Model 1 (29 residues), in which S^2 is the only parameter to fit. No model was assigned to E281. The resulting parameters, including errors, are represented in Supplementary Table S5. Twelve residues exhibit additional conformational exchange represented by the R_{ex} term (Supplementary Fig. S3A and Supplementary Table S5), which can indicate slow conformational changes in the protein. Compared to R_2 data, the R_{ex} term of most residues may be considered low except for R280, located in the C-terminal loop. Nine residues with R_{ex} are located in the N-terminal and C-terminal α-helices, suggesting these regions undergo specific conformational changes on a slow time scale, especially on α-helix 1. R_{ex} terms represent slow (microseconds to milliseconds) dynamics. The existence of the 12 R_{ex} terms identified by model-free analyses prompted us to investigate slow CTD backbone dynamics experimentally. We employed $R_1\rho$ rotating-frame relaxation experiments [48] and determined the CTD R_{ex} values by subtracting $R_1\rho$ from R_2 (Supplementary Fig. S4). The experimentally determined R_{ex} shows the presence of conformational changes on slower timescales in the N- and C-terminal α-helices, with the majority of identified residues having low R_{ex} (below 1.0 s^{-1}). Considering the SD errors, these experimentally determined R_{ex} results agree with the ones from the theoretical model-free analyses and show the presence of the slow dynamics at the CTD α-helices. The results of Model-Free analysis and $R_1\rho$ experiments suggest that CTD backbone does not experience extended conformational changes in the apo state while having mostly axially symmetric molecular tumbling.

S^2, τ_s, τ_e distribution of apo CTD reveals contrasting motions in the DNA-binding lysine residues

Most residues of apo CTD exhibit fast internal motion ($\tau_e \ll \tau_m$), and only the order parameter S^2 was needed to fit Model 1 (Supplementary Table S5). Supplementary Fig. S3B shows that the fast timescale (τ_e) motions were detected in the linker region (K255 and K256) and the surrounding β-strands. Relatively slower internal motions (τ_s) were detected predominantly in the N- and C-terminal residues, but also in the linker region (K257) (Supplementary Fig. S3C).

The order parameter values for angular motion (S^2) extracted from the Lipari–Szabo's model-free formalism [60] carry substantial weight in understanding ^{1}H-^{15}N bond vector internal motions [79]. Figure 2A, C, and Supplementary Fig. S5A and C display the S^2 values where 0 and 1 represent complete flexibility and rigidity, respectively. The overall average value of S^2 for apo CTD is 0.83 ± 0.20 (SD). The average values of S^2 for the secondary structural elements and termini regions in the apo CTD are listed in Table 1.

Twenty-six NH vectors in apo CTD exhibit $S^2 \geq 0.9$, of which six vectors have $S^2 \geq 0.95$. A high degree of motion restriction was observed in α-helix 1 and both β-strands. In α-helix 2 (266–279), its last two residues, S278 and E279, show highly elevated mobility (low S^2) for their NH vectors

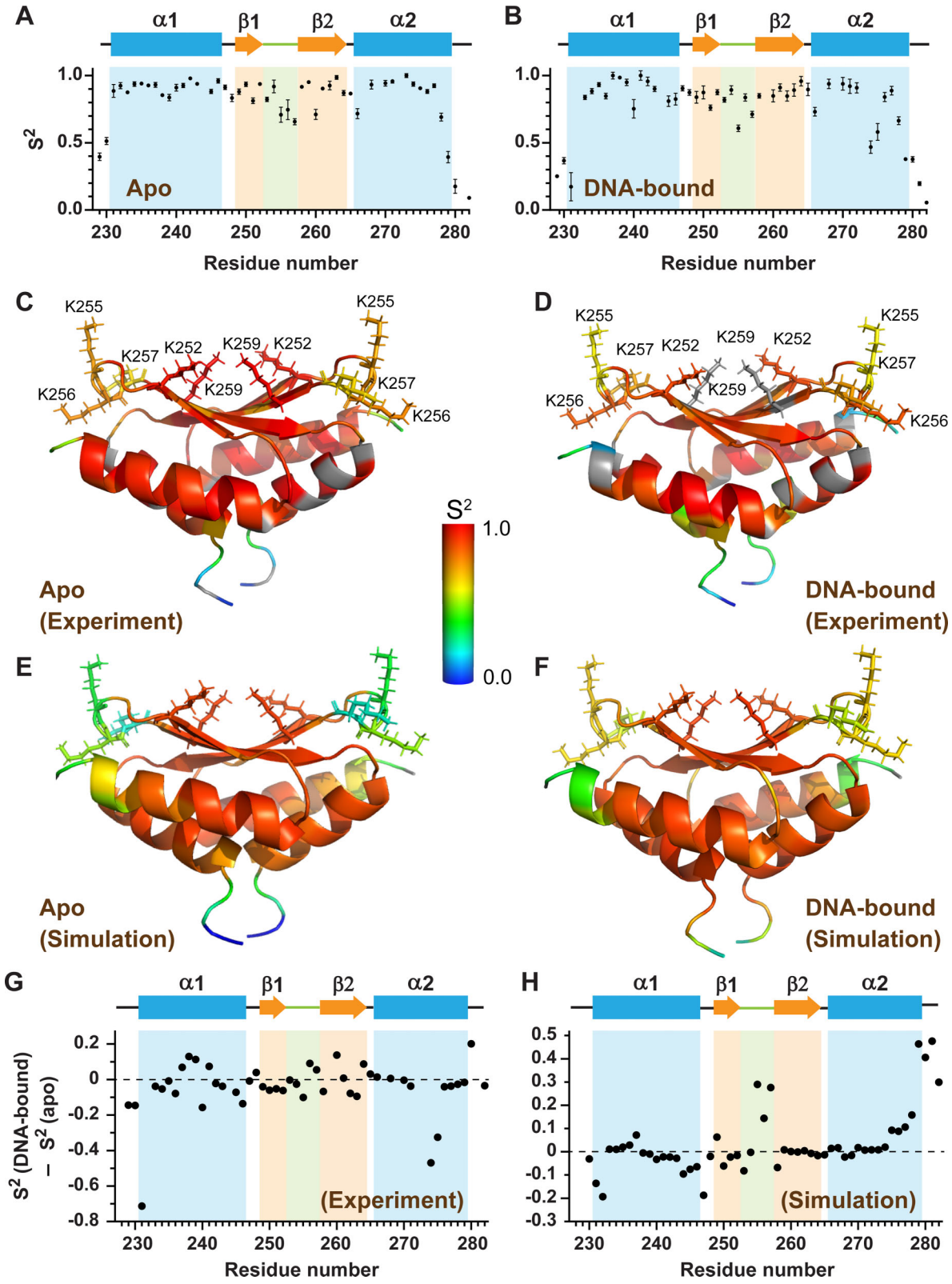

Figure 2. Calculated S^2 values and their differences upon DNA binding. (**A**, **B**) The order parameter, S^2, for apo and DNA-bound CTD, respectively. Error bars: SD. Calculated S^2 values from NMR relaxation experiments for (**C**) apo and (**D**) DNA-bound CTD, respectively. The color-coded values are mapped onto CTD structure (PDB entry: 5NOC). Lysines of interest are labeled. Color scheme: gradient from blue to red for residues with S^2 between 0.0 and 1.0, and gray for residues with no assigned S^2. Those from MD simulations for (**E**) apo and (**F**) DNA-bound CTD, respectively. Calculated S^2 value differences from (**G**) NMR experiment data and (**H**) MD simulation data, respectively. Positive and negative values imply enhanced and decreased rigidity, respectively, upon DNA binding.

(Fig. 2A), in contrast to the significantly restricted dynamics of the rest of α-helix 2. Both relaxation data (R_2/R_1 and NOE) and S^2 values for S278 and E279 show similar trends for the C-terminal end (280–282) (Fig. 1C and D), suggesting that S278 and E279 might not belong to α-helix 2. Apart from these two residues, the general trend for the apo CTD is that both helices are the least dynamic (highly restricted motions), followed by the β-strands.

In contrast, outside of termini regions where the lowest average S^2 values are expected, the average value of S^2 is lowest (most flexible) for the linker loop (253–257) [0.77 ± 0.10 (SD)], where putative DNA-binding lysine residues are positioned (Fig. 2A and C; Supplementary Fig. S5A and C). K257 exhibits a particularly low S^2 value (0.657). In summary, lysine residues (K255–K257) on the flexible linker region show high flexibility (low S^2), while those on rigid β-strands (K252 and K259 on β-strands 1 and 2, respectively) show high rigidity (high S^2). It suggests distinct, location-dependent roles for each lysine residue, as we discuss later.

Relaxation data show altered backbone dynamics upon DNA binding

Since positively charged amino acid patches on CTD have been known to bind DNA nonspecifically [33], we investigated structural aspects of DNA-bound CTD using NMR relaxation data acquired in the same manner as for the apo CTD. To determine the shift of signals, we titrated CTD with DNA in 0.25 equivalent steps up to 1.25 equivalents as in [33] to saturate protein and collected ^{1}H-^{15}N HSQC for each step (Supplementary Figs S2B and S6). Several peaks were excluded from the relaxation data due to significant line broadening or peak overlap. All relaxation parameters were plotted as a function of the amino acid residues and are reported in Fig. 1E–H. (see also Table 1.) The initial mean correlation time (τ_m) was 15.45 ± 1.10 (SD) ns, and the mean R_2/R_1 ratio was 13.84 ± 6.60 (SD). Calculations were performed as described in the "Materials and methods" section. While R_1 of the apo CTD exhibits similar values across the chain, the R_1 data of the DNA-bound CTD shows a marked decrease for the secondary structures (Fig. 1A and E). On the other hand, the R_2 of the DNA-bound CTD exhibits a significant increase in its values along the secondary structures (Fig. 1B and F). R_2/R_1 for the DNA-bound CTD significantly increases along the whole chain except for the termini (Fig. 1G). This indicates a slowing down of molecular tumbling due to DNA binding. While we observed the global increase in R_2/R_1 by adding DNA to the CTD, the R_2/R_1 patterns in the DNA-bound CTD are somewhat different compared to the apo CTD. Upon binding to the DNA, both β-strands, which participate in the DNA-binding through K252 and K259, have R_2/R_1 values that are lower or almost the same as the average R_2/R_1 (16.600), while in the apo-CTD, the R_2/R_1 of the β-strands are above the average, indicating dynamic changes introduced by DNA. Additionally, both helices in the DNA-bound CTD exhibit higher than average R_2/R_1 ratios, indicating slower dynamics. However, in the apo state, the C-terminal α-helix's R_2/R_1 is below average. Only the dynamics of both loops and the linker are the same as in the apo CTD; the loops, especially the first, have slow motion, while the linker has fast dynamics. These data indicate that DNA induces dynamic changes to the CTD, and that the linker enables DNA recognition.

Determining DNA-bound CTD's dynamic parameters (S^2, R_{ex}, τ) with Model-Free analysis

Despite no DNA-bound structure of CTD being presently available, we decided to evaluate the dynamics of the DNA-bound CTD using the available apo CTD structure (PDB: 5NOC). As in the case of the apo CTD relaxation data analysis above, we determined a motional model for the DNA-bound CTD (Supplementary Table S6). The molecular tumbling of DNA-bound CTD was best described as fully anisotropic with D_A equal to 1.319 ± 0.074 (SD) ($\chi^2 = 22.83$, $F = 1.69$). The average overall rotational correlation time, τ_m, was 15.23 ± 0.23 (SD) ns. Compared to apo CTD, the degree of anisotropy of DNA-bound CTD is more considerable. Nonetheless, this anisotropy is still not large, so we can treat the tumbling of DNA-bound CTD as axially symmetric, applying the output pdb file for anisotropic diffusion analysis. The results (and their error information) of using axially symmetric models for rotational diffusion tensors show that the relaxation of NH vectors of the majority of the DNA-bound CTD residues fit the simplest Model 1 (36 residues) (Supplementary Table S7). Two residues were not assigned (A232 and I273). In contrast to apo CTD, only three residues (D231, Y240, and E275) exhibit additional conformational exchange represented by R_{ex} term (Supplementary Fig. S3D and Supplementary Table S7). The results of Model-Free analysis suggest that the addition of DNA decreases conformational changes of CTD backbone in comparison to apo CTD.

S^2, τ_s, τ_e distribution of DNA-bound CTD reveals changes in the dynamics of DNA-binding lysine residues upon addition of DNA

As with apo CTD, the majority of residues in the DNA-bound CTD exhibit fast internal motion and require only S^2 to fit Model 1 (Supplementary Table S7). Comparisons between Supplementary Fig. S3B and E show that the fast timescale (τ_e) internal motion becomes slower in the linker region (K255 and K256) when DNA is bound. As in apo CTD, relatively slower internal motions (τ_s) were detected predominantly in the N- and C-terminal residues but also in the linker region (K257) (Supplementary Fig. S3F).

Figure 2B, D, and Supplementary Fig. S5B and D display the order parameter for angular motion, S^2. The overall average value of S^2 is 0.76 ± 0.24 (SD) (see also Table 1). Outside of termini regions, the average values of S^2 are smallest for α-helix 2 [0.75 ± 0.19 (SD)] and the linker (253–257) [0.77 ± 0.11 (SD)] (Fig. 2B, D, and Supplementary Fig. S5B and D). DNA binding resulted in S^2 value changes throughout the CTD structure (Fig. 2G). Introducing DNA has prominent consequences on S^2 values, including (i) more restricted internal motion (higher S^2) in the middle of α-helix 1 and decreased S^2 on both of its ends, (ii) increased flexibility (lower S^2) on β-helix 1, and (iii) lower and higher rigidities (lower and higher S^2) for K255 and K256–K257 linker lysine residues, respectively. These results suggest different roles of K255 and K256/K257 in DNA recognition, which warrants further investigation.

E261-mediated salt bridges hold two CTD monomers together

The flexible linker region contains three putative DNA-binding lysine residues (K255–K257). We claim that the elevated dynamics of the linker are essential for DNA recogni-

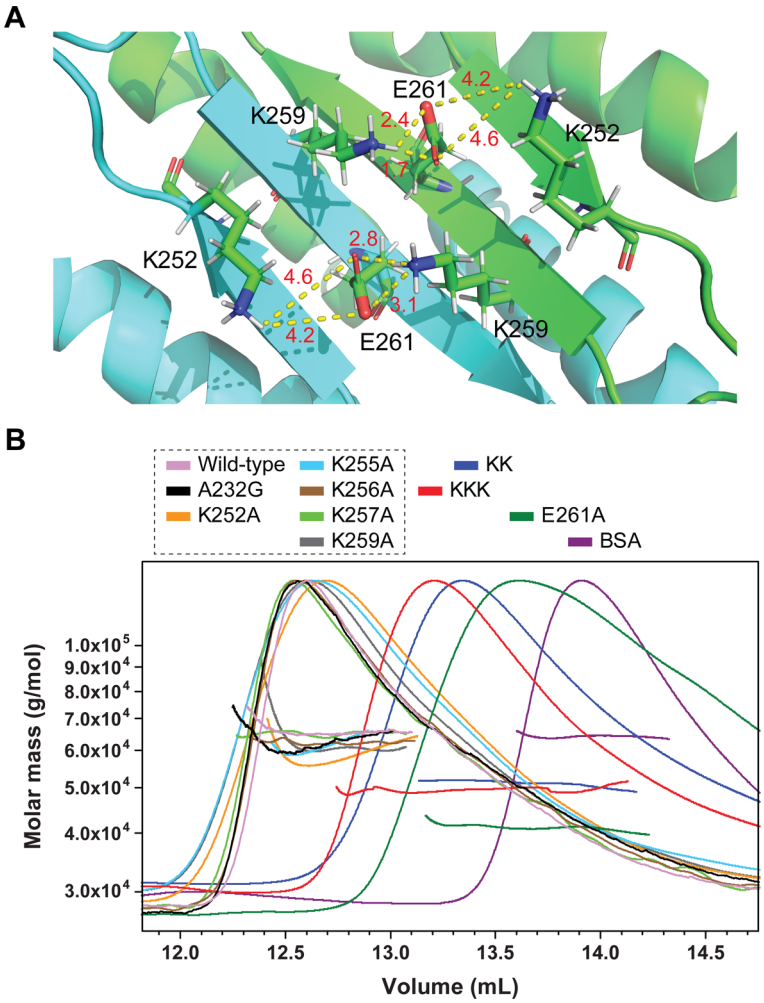

Figure 3. Salt bridge disruptions substantially weaken dimerization of the CTD. (**A**) PyMol representation of salt bridge network formed by K252, K259, and E261 (PDB: 5NOC). Green and cyan colors represent each CTD monomer. Numbers in red are distances in angstroms. (**B**) SEC-MALS characterization of WT and mutant ParB proteins. Light scattering signals are represented in the Rayleigh ratio. Signals were monitored using SEC-MALS and normalized to the maximum in each curve. 0.1 ml of 0.02 mM samples were injected with 20 mM Tris, 350 mM NaCl running buffer at pH 8.0. KK: K252A–K259A, KKK: K252A–K255A–K259A.

tion. Other putative DNA-binding lysine residues (K252 and K259) are located on highly rigid (high S^2) β-strands. We questioned whether there were any structural grounds for the high rigidity of K252 and K259 residues and investigated surrounding residues from the known structure of apo *B. subtilis* ParB CTD (PDB: 5NOC) [33]. We discovered that negatively charged E261 on β-strand 2 forms salt bridges with K252 on the same CTD monomer and K259 on the other monomer (Fig. 3A). These salt bridges confer the high rigidity of the K252 and K259 residues and imply different roles for lysines within β-strands (K252 and K259) compared to those within the linker region (K255–K257) (see "Discussion" section).

The intra- and inter-monomer salt bridges mediated by E261 raised the possibility that those salt bridges play an instrumental role in CTD dimerization. We hypothesized that mutating E261 into alanine would disrupt the dimeric status of BsParB proteins. To investigate the monomer-dimer status of BsParB proteins, we employed SEC-MALS (Fig. 3B). A control experiment with BSA (66.5 kDa) correctly provided the molecular weight (64.2 kDa with 0.4% uncertainty) of its monomeric form (the major peak). As was observed from other ParB studies [31, 32, 80], the (full-length) WT BsParB in solution was eluted as a single peak with a calculated molecular weight of 65.7 kDa (uncertainty: 1.2%), which matches a theoretical dimeric molecular weight. However, the SEC-MALS measurements with BsParB(E261A) yielded a molecular weight of 41.1 kDa (with 2.0% uncertainty), which is clearly lower than the dimer's molecular weight (~64 kDa) and slightly higher than the monomer's (~32 kDa). These results imply that BsParB(E261A) is primarily a monomer. While it runs through the size exclusion column, the two monomers can weakly and temporarily associate with each other. Our MALS system measures the average molecular weight of the monomer (major) and weakly associated dimer (minor) populations. The measured molecular weight of BsParB(E261A) proves our hypothesis that E261 is a key residue involved in the CTD dimerization. On the other hand, mutations on the lysine residues (K252A, K255A, K256A, K257A, and K259A) did not compromise the dimeric status of BsParB (59.0, 61.3, 62.4, 65.2, and 62.5 kDa with 2.4%, 2.2%, 1.5%, 1.6%, and 6.1% uncertainties, respectively) (Fig. 3B). The SEC-MALS results imply importance of the intra- and inter-monomer salt bridges mediated by E261 for CTD

dimerization and raise questions about their roles in protein function.

Molecular dynamics simulations of apo and DNA-bound CTD reveal conformational changes in the protein upon DNA binding

The absence of crystal or NMR structures for the DNA-bound CTD prompted us to perform MD simulations of apo and DNA-bound CTD using GROMACS software. After equilibration procedures (Supplementary Fig. S7A–F), the MD simulation determined the order parameter S^2 values (Fig. 2E and F). These values were compared with the experimentally obtained S^2 values. In addition, we obtained and compared the average structures for the simulated apo- and DNA-bound CTD (Supplementary Fig. S8A–D).

During 500 ns of simulation under identical conditions, both apo and DNA-bound CTD preserved their structural stability. We used variable averaging times (100 ps to 5 ns) to extract S^2 order parameters from the MD trajectories (Supplementary Tables S8 and S9). The S^2 values derived from MD for both the apo and the DNA-bound CTD are generally close to agreement with experimentally derived S^2 (Supplementary Fig. S9A and B): (i) elevated mobility (lower S^2) within the linker area (residues 253–257) and the termini, and (ii) elevated rigidity (higher S^2) within the rest of the backbone chain. The MD-derived S^2 values for the apo CTD correctly predict K257 as the most flexible lysine residue outside of the termini regions, corroborating the NMR relaxation results. However, we noted that MD exaggerates internal motion (low S^2) at the linker region, particularly in the apo CTD (Supplementary Fig. S9A and B). The exaggerations of NMR S^2 values for flexible protein residues are a well-known feature of MD simulations [81, 82].

The general patterns of DNA-binding effects on the S^2 values were approximately reproduced in the MD simulations, except for the C-terminal half of α-helix 2 and the C-termini (Fig. 2G and H). First, positive "S^2(DNA-bound)-S^2(apo)" values in the middle of α-helix 1 and negative values from both ends of α-helix 1 were also obtained in the simulations, although the magnitude of the S^2 value changes in the MD simulation was less pronounced. Consistent with experimental data, increased flexibility (lower S^2) on β-helix 1 upon DNA binding was observed, and the internal backbone rigidities for K256–K257 were increased upon DNA binding. However, contrary to the experimental data, DNA binding increased the K255 backbone rigidity in the simulation.

The comparison of the simulated CTD structures in the absence and presence of DNA (Supplementary Fig. S8A–D) shows that α-helices of DNA-bound CTD are out of the center of symmetry. Also, while the β-strands of both the DNA-bound and the apo-CTD are closely overlaid in the simulation, the first β-strand of the DNA-bound CTD is shorter, extending the coil-like linker regions. Interestingly, compared with the NMR structure of CTD (PDB: 5NOC), the first β-strand in both the apo and DNA-bound simulated structures appears longer (Supplementary Fig. S8E). The second β-strands in 5NOC and DNA-bound simulated structures exhibit the same length but are similarly shorter than the simulated apo structure (Supplementary Fig. S8E). We argue that the shortening of β-strands of DNA-bound CTD in MD simulations is probably due to the critical importance of decreased structural constraint for DNA recognition and sliding. However, due to the lack of DNA-bound NMR or crystal structures of CTD or the full-length ParB, the results should be interpreted with caution by comparing only simulated apo and DNA-bound CTD structures. The results of MD simulations allowed us to "theoretically" observe the conformational changes upon DNA binding to the CTD and suggest that DNA modulates the structure of CTD by shortening the β-strands.

Mutating individual CTD lysine residues significantly reduces single-molecule DNA compaction rates

In NMR, CSP is a powerful and sensitive tool in investigating structural changes upon ligand binding [83]. Consistent with the previous results by Fisher *et al.* [33], our CSP results show that K252, K255, K256, and K259 lysine residues, along with A232 in α-helix 1 (231–246), experience high perturbation upon DNA binding (Supplementary Fig. S10). Among them, K256 shows the highest CSP (0.297), and K255 exhibits a marginally high CSP (0.083). In contrast, DNA binding does not yield a noticeable chemical shift perturbation on K257 in the loop region (253–257) (see reference [33] and Supplementary Fig. S10).

To understand how key CTD residues contribute to the overall function of the ParB protein, we employed a single-molecule DNA flow-stretching assay. Single-molecule DNA flow-stretching is a widely employed, versatile methodology in DNA–protein interaction studies [84]. Its high sensitivity allows detection of even minor changes in proteins of interest by monitoring end-to-end length changes of flow-stretched DNA [43]. In this assay, one end of the 48.5-kb bacteriophage λ-DNA was tethered to a microfluidic sample chamber surface, and the other end was labeled with a fluorescent quantum dot. Applying laminar buffer flow leads to DNA stretching and delivers proteins to the flow-stretched DNAs. The bridging activities of DNA-ParB or ParB-ParB [32, 38, 42] result in end-to-end length changes of flow-stretched DNA, which are visualized by monitoring the quantum dot position over time [32, 38, 42, 80, 85–87].

The compaction rates of flow-stretched DNA of the full-length WT BsParB were compared with those of (full-length) mutant ParB proteins. First, BsParB(A232G), BsParB(K252A), BsParB(K255A), BsParB(K256A), and BsParB(K259A) were tested, as residues participating in direct DNA binding or undergoing conformational changes upon DNA binding are expected to have large CSP values [83]. Despite its low CSP, BsParB(K257A) was another mutant we tested due to its particularly high backbone flexibility (low S^2). BsParB(E261A) was also chosen to investigate the effects of the disruptions of salt bridges between E261 and rigid K252/K259 residues.

Consistent with the results in our previous publication [43], 50 nM WT BsParB robustly compacted flow-stretched DNA in the absence of CTP ($n = 31$) and showed substantial compaction rate decreases in the presence of CTP ($n = 52$) (Fig. 4A and B and Supplementary Table S10). In our current study, since our goal is to understand BsParB's nonspecific DNA-binding activity, we used bacteriophage λ-DNA, which lacks any *parS* sequences, as the DNA substrate. Along the same lines, the previous single-molecule DNA flow-stretching work showed that a CTP-induced substantial decrease in the DNA compaction rate is a common feature, even when an engineered bacteriophage λ-DNA with a single *parS* sequence in the middle is used [43]. In contrast, CTP promotes DNA

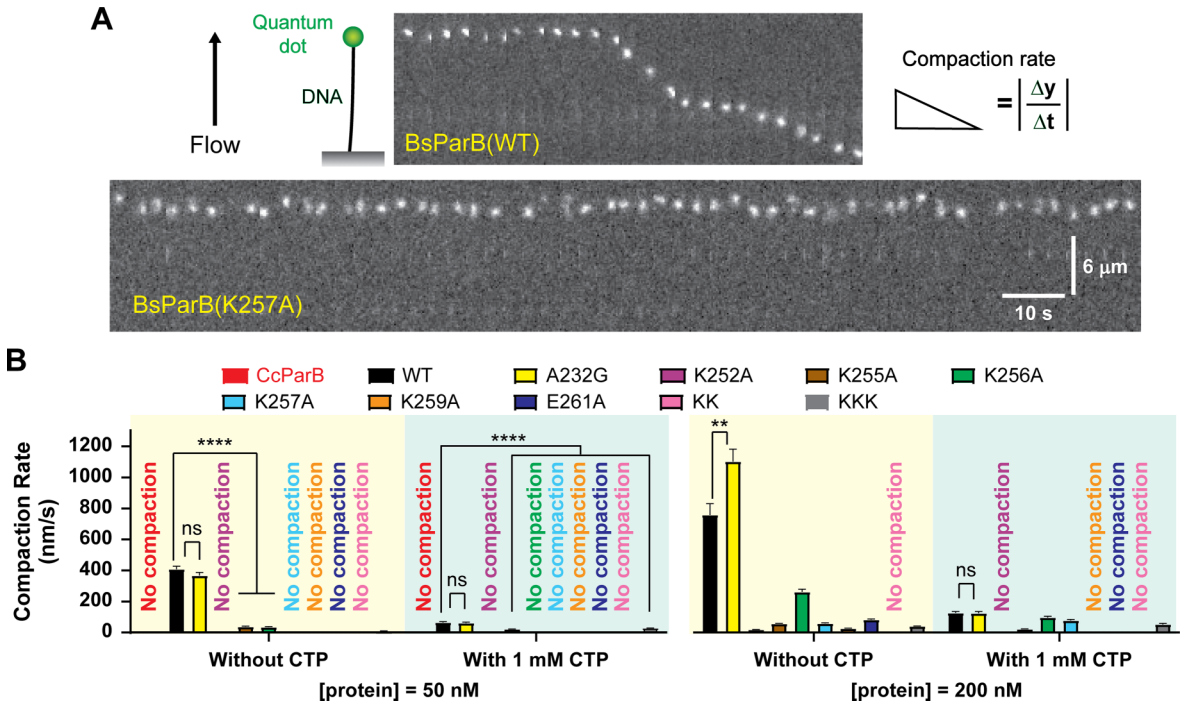

Figure 4. The CTD lysine mutations decrease the compaction rates of single-molecule flow-stretched DNAs. (**A**) Schematic of single-molecule DNA flow-stretching assay. The two kymographs for the WT and the K257A mutant *B. subtilis* ParB represent efficient and no DNA compaction events, respectively. (**B**) DNA compaction rates by various ParB proteins (50 and 200 nM) both in the presence and absence of CTP ($n = 23$–234). CcParB stands for *C. crescentus* ParB, which lacks the CTD lysine patches. Other proteins are *B. subtilis* ParB. Error bars: standard error of the mean (SEM). Despite the presence of multiple lysines, a single lysine mutation results in a decrease in the DNA compaction rates. Mann–Whitney test was employed. ns: not significant, **: $.001 < P < .01$, ****: $P < .0001$.

compaction in a single-molecule magnetic tweezer assay [41]. However, those two results are not mutually contradictory. In the flow-stretching assay, there is only one *parS* (16 bp) in the 48.5 kbp λ-DNA. However, in the magnetic-tweezer assay, the 6.9 kbp DNA substrate contains 13 *parS* sites (208 bp). Therefore, the interaction between nonspecific DNA and ParB is more emphasized in the DNA flow-stretching assay, whereas the specific interaction between *parS* sites and ParB is more pronounced in the magnetic tweezer assay [88]. In fact, when CTP was present, our previous DNA flow-stretching assay showed a modest recovery in DNA compaction rates with the engineered 1-*parS* λ-DNA, with the difference being statistically significant ($P < .0001$) [43].

The 50 nM BsParB(A232G) mutant protein behaved similarly to the WT BsParB with statistically insignificant compaction rate differences ($n = 30$ without CTP and $n = 43$ with CTP) (Fig. 4B). However, regardless of CTP, *C. crescentus* ParB (CcParB), which lacks the CTD lysine patches [13, 14], did not compact DNA ($n = 34$–35) (Fig. 4B). We observed that single-lysine mutant proteins at 50 nM lost substantial DNA compaction capability. No compaction events were observed for BsParB(K252A), BsParB(K257A), and BsParB(K259A) regardless of CTP or for BsParB(K256A) in the presence of CTP (Fig. 4A and B). Even for 50 nM BsParB(K256A) without CTP, the compaction rate was 12-fold slower than that of WT BsParB ($P < .0001$; Mann–Whitney test). The 50 nM BsParB(E261A) protein, in which salt bridges are disrupted, also did not compact flow-stretched DNA ($n = 77$–83) (Fig. 4B).

Next, we analyzed how lysine point mutations affect DNA compaction rates of the engineered bacteriophage λ-DNA harboring one *parS* site in the middle (1-*parS*-DNA). After confirming that CTP decreases the 1-*parS*-DNA compaction rates by WT BsParB as expected, we did the same measurements using BsParB(K256A) and BsParB(K259A). For BsParB(K256A), 21 out of 24 1-*parS*-DNA molecules showed DNA compaction (mean ± SEM = 3.5 ± 0.8 nm/s) in the absence of CTP. Intriguingly, the 1-*parS*-DNA compaction rate by BsParB(K256A) is lower than regular λ-DNA (without any *parS* sequence) compaction rate. This result is reminiscent of our previous observations that, when 1-*parS*-DNA was used, WT BsParB without CTP compacted DNA more slowly than when regular λ-DNA was used, showing a negative effect of *parS* on DNA compaction [43]. In the presence of CTP, 35 out of 37 1-*parS*-DNA molecules did not show DNA compaction by BsParB(K256A) at all. Although two molecules showed compaction, the rate was extremely low, at 0.5 ± 0.5 nm/s (mean ± SEM). This observation demonstrates CTP's inhibitory effects on DNA compaction by BsParB(K256A). When BsParB(K259A) was tested with 1-*parS*-DNA, no DNA compaction was observed both in the presence ($n = 14$) and absence of CTP ($n = 22$), as was observed with regular λ-DNA.

Considering that multiple putative DNA-binding lysine residues exist at the CTD, we wondered whether a single-point mutation could abolish DNA compaction even at an increased protein concentration. DNA flow-stretching experiments with four-fold increased protein concentration (200 nM) showed that BsParB(K255A), BsParB(K256A), BsParB(K257A), and BsParB(K259A) mutants retained DNA compaction abilities, albeit with significant disruption to DNA compaction rates ($P < .0001$; Mann–Whitney test) (Fig. 4B and

Supplementary Table S10). No DNA compaction was seen for 200 nM BsParB(K252A) with CTP. The substantial decrease in DNA compaction rates observed for the CTD mutants led us to question whether they were properly folded. However, the HSQC spectra of key CTD lysine mutants (K256A and K259A), compared to that of the WT CTD (Supplementary Fig. S11A–C), indicate that the CTD mutant protein misfolding is highly unlikely. Our results demonstrate the crucial roles of CTD lysines in DNA compaction, most likely by being involved in DNA bridging events. Slow DNA compactions by 200 nM BsParB(E261A) were seen only when no nucleotides were supplemented. Interestingly, whereas the compaction rate difference between WT and A232G BsParB in the presence of CTP was still statistically insignificant, the compaction rate of the 200 nM A232G BsParB was higher than the 200 nM WT protein in the absence of CTP ($.001 < P < .01$; Mann–Whitney test) (Fig. 4B and Supplementary Table S10). We attribute the compaction rate increase (without CTP) to a minor conformational change induced by the A232G mutation. The conformational change may lead to more protein loading on a flow-stretched DNA. However, we speculate that the change is so subtle that it is noticeable only with the 200 nM A232G (but not with 50 nM concentration.) In summary, mutating individual lysines dramatically disrupts DNA compaction (even though the remaining lysines are intact) (see "Discussion" section later).

The dramatic decreases in DNA compaction rate upon introduction of lysine point mutations prompted us to investigate the effects of these mutations on DNA binding using an electrophoretic mobility shift assay (EMSA). Taylor *et al.*'s work showed that using a buffer containing magnesium ions was essential to detect *parS* sequence-specific DNA-ParB interactions in EMSA [32]. Our current study focuses on nonspecific DNA–ParB interactions via CTD. To minimize DNA–ParB interaction through the helix-turn-helix motif on CDBD (Supplementary Fig. S1A), we omitted magnesium ions and used 169-bp dsDNA, which lacks *parS* sequences, in our EMSA experiments. At 1 μM protein concentration, the WT ParB exhibited efficient gel shift (Supplementary Figs S12A and S13A). Other ParB proteins with single-lysine mutations still bound DNA, but binding was less efficient than that of the WT protein. To strengthen our observations, EMSA was repeated with increasing concentrations of WT, K256A, and K259A proteins (Supplementary Figs S12B–D and S13B–D). While a noticeable gel shift with WT ParB was detected even at 0.3 μM concentration, applying 0.7 μM of BsParB(K256A) and 1.0 μM of BsParB(K259A) was needed to see comparable degrees of gel shifts, indicating mildly decreased DNA affinity.

K256A or K257A mutation does not affect fluorescent ParB foci formation *in vivo*

To investigate how ParB's DNA compaction capability *in vitro* correlates with ParB's cellular localization and foci formation *in vivo*, we performed live-cell fluorescence imaging for *B. subtilis* strains harboring various mutant ParB proteins. GFP was tagged to the N-terminus of WT or mutant ParB, and the construct was expressed from an ectopic locus on the chromosome in which the endogenous *parB* gene was deleted [38, 43]. Previous studies have shown that WT GFP-ParB forms nucleoprotein complexes that appear as fluorescent foci [10, 11, 19, 33, 38, 40, 43, 80, 89–91], while the BsParB(R80A) mutant exhibits diffusive localization [38, 43, 80]. Fluorescent foci formation has been considered to represent *in vivo* ParB spreading in *B. subtilis* [38, 80]. Consistent with previous work, we found that WT GFP-BsParB showed clear foci, while GFP-BsParB(R80A) failed to form foci (Fig. 5A). We used these two strains as a positive control and a negative control, respectively. Consistent with the *in vitro* results that BsParB(A232G) compacted DNA similar to the WT (Fig. 4B), fluorescent foci formations were similar for WT BsParB and BsParB(A232G) in cells (Fig. 5A). For the salt bridge-disrupted BsParB(E261A) mutant, fluorescence foci formation was intermediate between those for WT GFP-BsParB and GFP-BsParB(R80A). Foci-like signals from GFP-BsParB(E261A) were still detected, but fuzzy and faint. Strikingly, bright GFP-BsParB(K255A), GFP-BsParB(K256A), and GFP-BsParB(K257A) foci were observed *in vivo* (Fig. 5A and B), in contrast to the poor flow-stretched DNA compaction by BsParB(K256A) and BsParB(K257A) observed *in vitro* (Fig. 4B). These results suggest that for major defects in protein structure, *in vitro* DNA compaction assay and *in vivo* fluorescence foci formation show consistent results. However, *in vitro* DNA compaction assay is more sensitive than *in vivo* foci formation in capturing subtle protein structure changes. (see more in "Discussion" section).

CTD dimerization is required for ParB's *in vivo* activities

We noticed that the dimeric BsParB(A232G), BsParB(K255A), BsParB(K256A), and BsParB(K257A) proteins form distinct *in vivo* nucleoprotein complexes like the WT counterpart, while dimerization-perturbed BsParB(E261A) entails noticeable foci disruptions (Fig. 5A). Based on these *in vivo* live cell imaging and SEC-MALS results, we hypothesized that ParB protein dimerization via the CTD is essential for ParB protein actions *in vivo*.

We first attempted to identify other CTD mutations that affect dimerization. Given that E261 forms salt bridges with K252 and K259, we purified BsParB(K252A–K259A) [hereafter "BsParB(KK)"] and BsParB(K252A–K255A–K259A) [hereafter "BsParB(KKK)"] to investigate their monomeric/dimeric statuses using SEC-MALS. The HSQC spectra comparison confirmed that the purified KKK CTD protein is properly folded (Supplementary Fig. S11A and D). We did not include the monomer candidate BsParB(L270D–L274D), where leucine zipper-mediated dimerization is abrogated, because it has been reported that this mutant is insoluble upon overexpression [33].

The molecular weights of BsParB(KK) and BsParB(KKK) were measured to be 51.2 kDa (with 2.0% uncertainty) and 49.5 kDa (with 1.4% uncertainty), respectively (Fig. 3B), much smaller than the molecular weight of the ParB dimer (~65 kDa). These values suggest disruptions in CTD dimerization because dynamic monomer and dimer transitions result in intermediate molecular weight values in SEC-MALS experiments and elution as a single peak through the size-exclusion column. The DNA compaction abilities of those mutants were mostly lost ($n = 53–234$) (Fig. 4B), which can be ascribed to no or little DNA-binding (Supplementary Figs S12E and S13E). When 1-*parS*-DNA was used instead, no DNA compaction by BsParB(KKK) was seen both in the presence ($n = 23$) and absence of CTP ($n = 31$). Next, we investigated how these mutations affect the formation of fluorescent ParB foci in

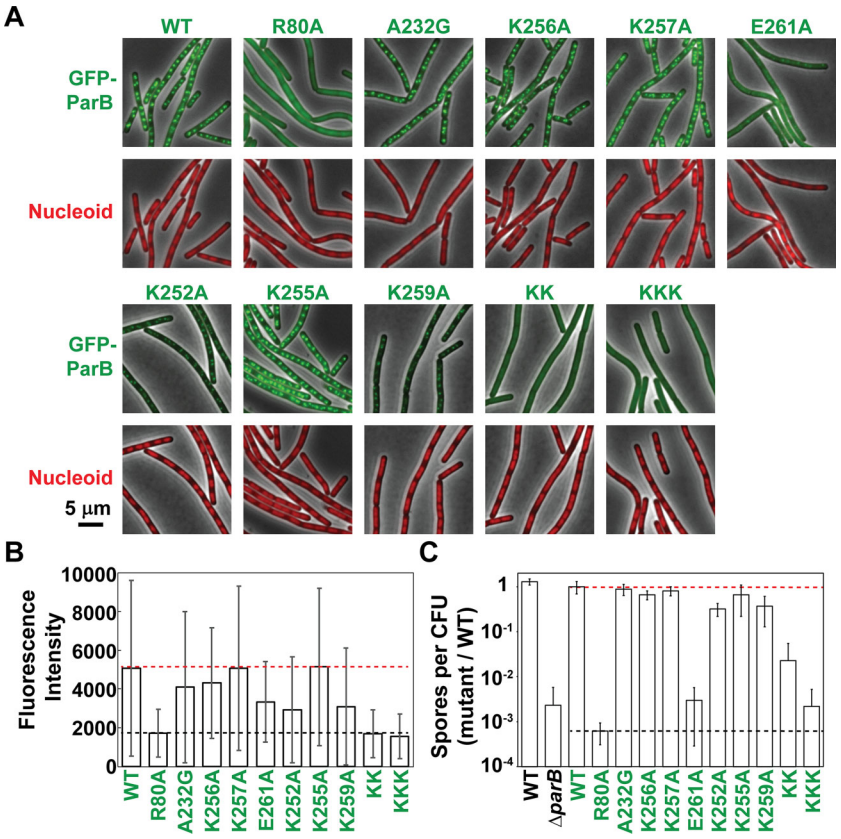

Figure 5. Disruption of CTD dimerization interferes with proper ParB foci formation and sporulation initiation. (**A**) Visualization of GFP-ParB variants. WT and R80A serve as a positive control and a negative control, respectively. The "KK" and "KKK" mutants contain K252A–K259A and K252A–K255A–K259A mutations, respectively. (**B**) Quantification of fluorescence intensity in panel (A). The mean pixel intensities were plotted as histograms after background subtraction. Error bars indicate the SD of pixel intensity. Red and black dotted lines indicate the fluorescence intensity of WT and R80A, respectively. (**C**) Sporulation efficiency (spore/CFU) relative to the GFP-BsParB WT strain. Green writing indicates the proteins that are tagged with GFP. Black writing indicates the WT and *ΔparB* mutant without GFP tags. Three biological replicates were averaged, and one SD was represented by the error bars. Error bars extending to the *x*-axis (as shown for *ΔparB*, "KK", and "KKK") indicate that zero was included within the range of the SD, which cannot be represented on a logarithmic scale. Red and black dotted lines indicate the sporulation efficiency of GFP-BsParB WT and R80A, respectively.

live cells. We found that *B. subtilis* cells harboring dimerized BsParB(K255A) formed foci that were comparable to the WT, while BsParB(K252A) or BsParB(K259A) also exhibited clear fluorescent foci, albeit weaker than the WT (Fig. 5A and B). However, foci formation was abrogated in BsParB(KK) and BsParB(KKK) (Fig. 5A and B), which is consistent with CTD dimerization disruptions.

Besides being important for chromosome segregation, ParB protein plays a critical role in initiating sporulation in *B. subtilis* [16], which is abolished by the R80A mutant [92]. To investigate whether the CTD mutations mentioned above impact spore formation, we analyzed sporulation efficiency (Fig. 5C). The sporulation efficiency of GFP-BsParB WT was similar to that of the WT strain without a GFP tag, indicating that GFP-BaParB is functional (Fig. 5C). As a negative control, we measured the sporulation efficiency for *ΔparB*, which is 0.23 ± 0.35% (mean ± SD) relative to the GFP-BsParB WT strain, consistent with previous results (~1.2%) [16]. Similar to *ΔparB*, GFP-BsParB(R80A) had a relative sporulation efficiency of 0.06 ± 0.03%. When the CTD mutations were introduced to endogenous *parB* locus and tested in the same way, the sporulation efficiencies of cells containing GFP-BsParB(A232G), GFP-BsParB(K256A), or GFP-BsParB(K257A) were comparable to the GFP-BsParB WT strain (89.0 ± 24.5%, 66.4 ± 14.9%, and 81.40 ± 18.60%, respectively.) For cells containing GFP-BsParB(K252A), GFP-BsParB(K255A), or GFP-BsParB(K259A), the sporulation efficiencies were slightly lower than the GFP-BsParB WT strain (Fig. 5C). Importantly, GFP-BsParB(E261A) (0.30 ± 0.27%), GFP-BsParB(K252A–K259A) (KK; 2.29 ± 3.21%), and GFP-BsParB(K252A–K255A–K259A) (KKK; 0.22 ± 0.30%) mutations reduced spore formation to a level similar to *ΔparB*. The trend in sporulation efficiency for these mutants is consistent with the trend in fluorescence foci formation (Fig. 5A and B).

Therefore, from SEC-MALS, *in vivo* live cell imaging, and sporulation assays, we discovered a prevalent trend: disruption of the ParB CTD dimerization, as seen from BsParB(E261A), BsParB(KK), and BsParB(KKK), is directly correlated with *in vivo* ParB activities seen in foci formation and sporulation initiation. Thus, the dimerization of the CTD is required for ParB's *in vivo* functions.

Discussion

Thermal fluctuations of structures allow proteins to continuously explore different conformational substates [63, 93].

It has been shown that protein backbone flexibility on the picosecond–nanosecond (ps–ns) timescale facilitates DNA-binding proteins in navigating nonspecific DNA [94]. In this study, we aimed to understand how these fast backbone dynamics (on the ps–ns time scale) of the lysine-rich DNA-binding CTD surface are translated into ParB functions using various *in vitro*, *in vivo*, and MD simulation approaches.

First, we used NMR relaxation approaches, which reveal ps–ns protein backbone dynamics with atomic resolution [93]. We show that the R_2/R_1 ratio along the CTD backbone is higher for the N-terminal half than for the C-terminal half (Fig. 1C and G), suggesting elevated conformational dynamics of secondary structures on the C-terminal side of the CTD in comparison to the N-terminal side. These results indicate that CTD has asymmetric structural and functional differences along its backbone. Interestingly, in the presence of DNA, the number of residues affected by the additional conformational exchange was reduced from 12 to 3, suggesting that DNA stabilizes the CTD structure. Upon DNA binding, NOE increases for secondary structures on the N-terminal side and on the linker but decreases for secondary structures on the C-terminal side of CTD (Fig. 1D and H), indicating that DNA binding elevates conformational dynamics within the C-terminal side.

The experimental data obtained from the NMR measurements were used to calculate the simulated order parameters (S^2) for residues in the CTD. We found that DNA-binding lysine residues exhibit different dynamics. The lysine residues on the linker region (253–257) show significant flexibility, while those on β-strands (K252 and K259) show high rigidity (high S^2). The rigid K252 and K259 not only participate in protein–DNA interaction, as observed from CSP data, but also in the dimerization of CTD by forming salt bridges with E261. These findings obtained from the experimental NMR are supported by our MD simulations, both showing that DNA–protein interface is formed by rigid and flexible regions. DNA slides along the rigid region with help from flexible lysine residues. These results show the importance of protein local dynamics in its function.

We found that single lysine mutations in ParB CTD (K252A, K255A, K256A, K257A, or K259A) exhibited substantially decreased DNA compaction rates in single-molecule DNA flow-stretching experiments, indicating that these lysine residues participate in nonspecific DNA binding and are important for *in vitro* DNA compaction. Consistent with this idea, *C. crescentus* ParB (CcParB), which lacks positively charged lysine patches at its CTD [13, 14], is incapable of compacting DNA *in vitro* (Fig. 4B), unlike ParBs from P1 plasmid, *Streptococcus pneumoniae*, *Pseudomonas aeruginosa*, *B. subtilis*, or ParB1 from *Vibrio cholerae,* which contain the lysine patches and are capable of compacting flow-stretched DNAs [38]. In the past, for BsParB(R80A) and many other *B. subtilis* mutants, the *in vitro* DNA compaction rates in the single-molecule DNA flow-stretching experiments were found to be coupled with *in vivo* fluorescence foci formation and sporulation [16, 38]. Surprisingly, single lysine mutations (K252A, K256A, K257A, or K259A) did not hamper the *in vivo* functions of *B. subtilis* cells as analyzed by fluorescence foci formation in live cells and sporulation efficiency. The weak correlation between *in vitro* DNA bridging and *in vivo* functions has also been reported in other mutants in a separate study [80]. Specifically, BsParB(M104A) and BsParB(Q140A) had reduced capability to compact DNA *in vitro* but formed fluorescence foci like the WT *in vivo* [80]. The inconsistency implies that the *in vitro* single-molecule DNA compaction assay is more sensitive in detecting changes in protein structure than *in vivo* assays.

Our results raise a question of how ParB's *in vivo* functions tolerate defects in interactions between DNA and ParB CTD. In *B. subtilis*, spore formation involves both ParA (Soj) and ParB (Spo0J) proteins [95]. Null mutations in *parB* lead to an 80–200-fold decrease in sporulation initiation (Fig. 5C and reference [16]) compared with the WT strain. Importantly, the *parA* null mutation suppressed the sporulation initiation defects caused by *ΔparB* [16] . Thus, it is the misregulation of ParA in *ΔparB* that causes sporulation defects [16, 95]. It has been shown that ParB's NTD interacts with ParA and stimulates ParA ATPase [1, 13, 14]. Thus, single lysine mutations within the CTD (K252A, K256A, K257A, or K259A) still allow ParB–ParA interactions. For *in vivo* fluorescence foci formation, despite the presence of nine *parS* sites on the *B. subtilis* chromosome [4], the WT GFP-ParB proteins appear as a single focus under fluorescence microscopy. Marston and Errington discovered that the absence of ParA leads to multiple smaller fluorescent ParB foci [96], suggesting that ParA proteins condense ParB–*parS* nucleoprotein complexes into one compact cluster [95, 96]. Our results are consistent with this idea, suggesting that *in vivo* ParA helps single CTD (dimeric) lysine mutants form fluorescent foci. Similarly, our previous study showed that adding a small KCK- or ECE-tag to ParB protein changes *in vitro* DNA compaction rates but does not alter *in vivo* foci formation or ParB distribution along the chromosome [43], which might also be explained by the help of ParA. Finally, it is also possible that other cellular factors, like molecular crowding and DNA supercoiling, allow mild DNA-binding defects to be tolerated. Future studies are needed to validate these possibilities.

Our *in vitro* single-molecule DNA flow stretching results (Fig. 4B) and live cell imaging and sporulation assays (Fig. 5A–C) showed that BsParB(E261A), BsParB(KK), and BsParB(KKK) exhibit strong defects in DNA compaction and *in vivo* functions. Those three mutants exhibit reduced CTD dimerization as judged by SEC-MALS (Fig. 3B). These results show that ParB dimerization via CTD is essential for *in vivo* ParB function and support the ParB sliding clamp model [20, 21, 30, 37, 41], where DNA is trapped in the compartment between the DNA-gate and the CTD.

The ParB sliding clamp model is reminiscent of the structure and function of proliferating cell nuclear antigen (PCNA), the DNA sliding clamp in eukaryotic cells. A ring-shaped homotrimer PCNA encircles DNA and plays a crucial role in DNA replication and damage repair [97]. Crystal structures of PCNA revealed that a central channel (inner rim) is lined with positively charged lysines and arginines to interact with the negatively charged DNA backbone (Fig. 6A) [98, 99], similar to the arrangement of lysine side chains on the ParB CTD. The basic (lysines and arginines) PCNA residues match the B-form DNA helix pitches. Short-lived polar interactions (on a sub-nanosecond timescale) between PCNA basic residues and DNA were proposed to facilitate PCNA sliding on DNA [100]. Inspired by the PCNA inner rim geometry, we inspected the DNA–ParB CTD interface using the CTD NMR structure (5NOC). We observe that the distances between lysines forming the DNA–ParB CTD interface are close to the dimensions of the major and minor grooves of DNA (Fig. 6B). The distance between the flexible lysines on the edge of the interface

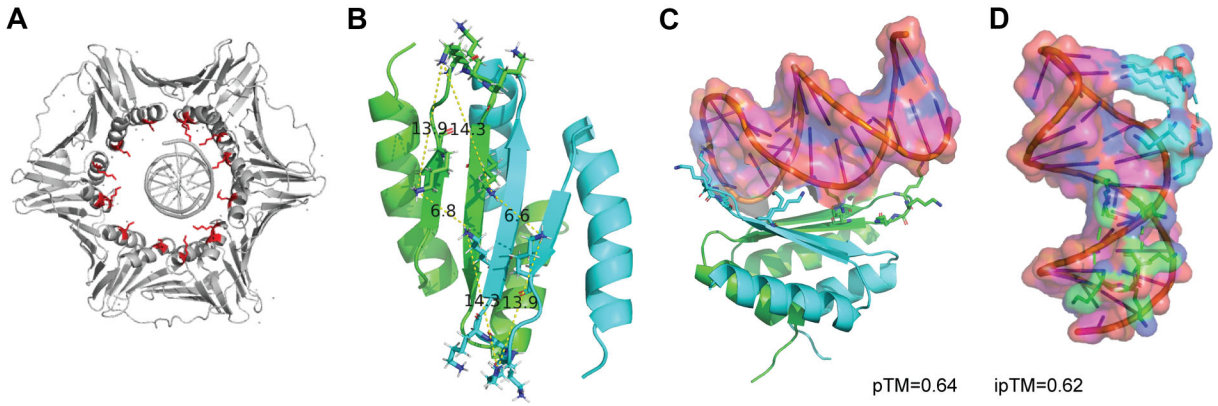

Figure 6. The configuration of the *B. subtilis* ParB CTD lysines enables the proper positioning of DNA. (**A**) A structure of human PCNA and associated DNA (PDB: 6GIS). The inner rim basic (lysines and arginines) residues are shown in red sticks. The arrangements and fast dynamics of these basic residues enable efficient DNA sliding. (**B**) The distances between lysine residues (stick representation) on *B. subtilis* ParB CTD (PDB: 5NOC) are shown in angstroms. Green and cyan colors represent different monomer CTDs. (**C**) AlphaFold 3 structure of DNA-bound ParB CTD. The ParB CTD lysines are aligned along the DNA backbone. pTM and ipTM refer to the predicted template modeling and the interface predicted template modeling scores, respectively. (**D**) Same as panel (C), but only lysine residues and the 10-bp DNA hairpin are shown at a different angle for clarity.

(K255–K257) and the lysines at the middle (K252 and K259) is approximately 14 Å, which fits inside the major groove of DNA (around 22 Å) [101]. The dimensions formed by four lysines at the center of the DNA–ParB CTD interfaces (K252 and K259 from each monomer) are between 6 and 7 Å, which fit inside the minor groove (around 12 Å) [101]. We propose that geometries formed by lysines at the DNA–CTD interface promote DNA sliding along the surface of the ParB CTD. Lastly, despite multiple DNA-interacting basic residues at the PCNA inner rim, mutating individual lysines or arginines to alanine leads to disruptions of PCNA-associated functions, such as the processivity of polymerase δ and the movement of PCNA on DNA [102, 103]. Those impacts were ascribed to the disruptions of clamp loading and the improper positioning of DNA along the basic PCNA inner rim residues [103]. Intriguingly, mutating only one ParB CTD lysine residue substantially lowered the single-molecule DNA compaction rates (Fig. 4B), whereas the affinity decreases between the ParB CTD and DNA is relatively mild (Supplementary Figs S12A–D and S13A–D). The origin of the dramatic effects from a single point mutation in the single-molecule assay is elusive, but the predicted DNA-BsParB CTD AlphaFold 3 [69] structure, where DNA is aligned along the CTD lysine residues, provides a hint (Fig. 6C and D). As proposed in PCNA, we speculate that the ParB CTD lysine residues collectively position a nonspecific DNA, so that the disruption of any of these lysine residues misaligns the DNA. Overall, our NMR S^2 and single-molecule results, along with inspiration from PCNA, suggest a "rail" mode of DNA non-specific binding where rigid (high S^2) K252 and K259 form an "inner guide," while flexible (low S^2) outer K255–K257 promote efficient DNA sliding.

In this study, we used *B. subtilis* as our model system. An alignment of ∼1800 ParB protein sequences indicates that the CTD has more sequence variability than the NTD and the CDBD [21]. Nevertheless, our and Jalal *et al.*'s sequence alignments (Supplementary Fig. S1B and reference [21]) show notable features about the CTD. The leucine residues for leucine zipper (L241, L270, L274, and L277 for *B. subtilis* [33]) are well conserved across chromosomal ParB. Although to a much lesser extent, some lysines (such as K256) are also conserved. Interestingly, as shown on the BsParB CTD (Fig. 2C–F and Supplementary Figs S5 and S14A), AlphaFold 3 structural predictions reveal that a subset of positively charged (lysine or arginine) residues in *Myxococcus xanthus, Vibrio cholerae*, and *Helicobacter pylori* are located in the compartment between the DNA-gate and the CTD (Supplementary Fig. S14B–D). In addition, as BsParB, single-molecule experiments with *Streptococcus pneumoniae*, *Pseudomonas aeruginosa*, *V. cholerae* ParB (or ParB1) proteins showed flow-stretched DNA compactions [38]. These observations suggest that lysine residues on the CTDs of other ParB species may play similar roles in DNA sliding. However, some ParB proteins, such as *C. crescentus* ParB (CcParB), lack positive lysine patches. Contrary to BsParB (and SpParB, PaParB, VcParB1), CcParB cannot compact flow-stretched DNAs (Fig. 4B). It is elusive how CcParB, which lacks CTD lysine patches and DNA compaction ability, efficiently slides along the DNA, forms a nucleoprotein complex, and plays an essential role in cell viability. Future studies on the CcParB CTD will shed light on how CTD-lysine-lacking ParB proteins perform their functions.

In summary, our NMR relaxation and MD studies reveal that CTD lysines exhibit distinct dynamics, facilitating nonspecific DNA binding to enable efficient ParB sliding along the DNA. Single-molecule approaches and AlphaFold 3-based structural prediction suggest that the integrity of all lysine residues is crucial for nonspecific DNA binding and its proper positioning. Any single lysine mutation significantly reduces the DNA compaction efficiency. However, single lysine mutations do not affect ParB's *in vivo* function, suggesting that other cellular factors, such as ParA–ParB interactions via NTD, molecular crowding, and DNA supercoiling, play a role. Only when ParB dimerization via the CTD is compromised [like in BsParB(E261A), BsParB(KK), and BsParB(KKK)], *in vivo* ParB functions are disrupted. Our results are consistent with the formation of ParB clamp after loading on *parS*. Our work sheds light on the mechanisms of ParB and reveals the impact of rapid protein dynamics on protein functions. Lastly, the remarkable similarities in the fast dynamics of ParB and PCNA raise questions about whether other DNA-binding proteins that move on DNA, such as DNA translocases and proteins involved in homology searches, adopt similar strategies.

Acknowledgements

We thank Kristin Cano from the University of Texas Health Science Center at San Antonio (UTHSCSA) for assistance with NMR spectroscopy. We thank Dennis Kwabiah for establishing the EMSA protocol, Candice Etson for providing the *E. coli* strain containing *parS*-lambda DNA, Thomas Graham for providing plasmids for BsParB wild-type, Alan Grossman for strains. NMR data presented herein were collected at the UTHSCSA Biomolecular NMR facility. We acknowledge the Texas Advanced Computing Center (TACC) at the University of Texas at Austin for providing computational resources.

Author contributions: Aleksey Aleshintsev (Conceptualization [equal], Data curation [equal], Formal analysis [equal], Methodology [equal], Writing—original draft [equal]), Lindsey E. Way (Data curation [equal], Formal analysis [equal], Methodology [equal], Writing—original draft [equal]), Ngoc Khanh Lai (Data curation [equal], Formal analysis [equal]), Bianca Guerra (Data curation [equal], Formal analysis [equal], Methodology [equal], Writing—original draft [supporting]), Paloma Dorantes (Data curation [equal], Formal analysis [equal]), Lois Akosua Serwaa (Data curation [equal], Formal analysis [equal], Methodology [equal]), Sealtiel Anulao (Data curation [equal]), Miranda Molina (Data curation [supporting], Methodology [supporting]), Xindan Wang (Conceptualization [equal], Funding acquisition [equal], Project administration [equal], Supervision [equal], Writing—original draft [equal]), HyeongJun Kim (Conceptualization [equal], Funding acquisition [equal], Project administration [equal], Supervision [equal], Writing—original draft [equal])

Supplementary data

Supplementary data is available at NAR online.

Conflict of interest

None declared.

Funding

This work was supported by the National Institutes of Health [R01GM141242, R01GM143182, R01AI172822 to X.W.; R35GM143093 to H.K.]. This research is a contribution of the GEMS Biology Integration Institute, funded by the National Science Foundation DBI Biology Integration Institutes Program [2022049 to X.W.]. Funding to pay the Open Access publication charges for this article was provided by the National Institute of General Medical Sciences [R35GM143093].

Data availability

The raw gel images are available in Supplementary Figs S1D and S12A–E. Raw single-molecule data, a summary of NMR data, and information about plasmids, oligos, and bacterial strains are provided in the supplementary tables. The raw data, along with T_1, T_2, and NOE data from the NMR relaxation study, have been deposited in the Biological Magnetic Resonance Data Bank (BMRB) under BMRB ID numbers (accession numbers) 53263 and 53264 for DNA-bound and apo results, respectively. We also deposited raw data, along with $T_{1\rho}$ data from the NMR relaxation study for apo, under BMRB ID 53455. The detailed data are available by reasonable request. The custom MATLAB codes used in the single-molecule data analyses are available from our previous publication [67].

References

1. Leonard TA, Butler PJ, Löwe J. Bacterial chromosome segregation: structure and DNA binding of the Soj dimer–a conserved biological switch. *EMBO J* 2005;24:270–82. https://doi.org/10.1038/sj.emboj.7600530
2. Roberts MAJ, Wadhams GH, Hadfield KA *et al.* ParA-like protein uses nonspecific chromosomal DNA binding to partition protein complexes. *Proc Natl Acad Sci USA* 2012;109:6698–703. https://doi.org/10.1073/pnas.1114000109
3. Lin DCH, Grossman AD. Identification and characterization of a bacterial chromosome partitioning site. *Cell* 1998;92:675–85. https://doi.org/10.1016/S0092-8674(00)81135-6
4. Breier AM, Grossman AD. Whole-genome analysis of the chromosome partitioning and sporulation protein Spo0J (ParB) reveals spreading and origin-distal sites on the *Bacillus subtilis* chromosome. *Mol Microbiol* 2007;64:703–18. https://doi.org/10.1111/j.1365-2958.2007.05690.x
5. Livny J, Yamaichi Y, Waldor MK. Distribution of centromere-like parS sites in bacteria: insights from comparative genomics. *J Bacteriol* 2007;189:8693–703. https://doi.org/10.1128/JB.01239-07
6. Ptacin JL, Lee SF, Garner EC *et al.* A spindle-like apparatus guides bacterial chromosome segregation. *Nat Cell Biol* 2010;12:791–8. https://doi.org/10.1038/ncb2083
7. Lim HC, Surovtsev IV, Beltran BG *et al.* Evidence for a DNA-relay mechanism in ParABS-mediated chromosome segregation. *eLife* 2014;3:e02758. https://doi.org/10.7554/eLife.02758
8. Surovtsev IV, Campos M, Jacobs-Wagner C. DNA-relay mechanism is sufficient to explain ParA-dependent intracellular transport and patterning of single and multiple cargos. *Proc Natl Acad Sci USA* 2016;113:E7268–76. https://doi.org/10.1073/pnas.1616118113
9. Hu L, Vecchiarelli AG, Mizuuchi K *et al.* brownian ratchet mechanism for faithful segregation of low-copy-number plasmids. *Biophys J* 2017;112:1489–502. https://doi.org/10.1016/j.bpj.2017.02.039
10. Sullivan NL, Marquis KA, Rudner DZ. Recruitment of SMC by ParB–parS organizes the origin region and promotes efficient chromosome segregation. *Cell* 2009;137:697–707. https://doi.org/10.1016/j.cell.2009.04.044
11. Gruber S, Errington J. Recruitment of condensin to replication origin regions by ParB/SpoOJ promotes chromosome segregation in *B. subtilis*. *Cell* 2009;137:685–96. https://doi.org/10.1016/j.cell.2009.02.035
12. Murray H, Errington J. Dynamic control of the DNA replication initiation protein DnaA by Soj/ParA. *Cell* 2008;135:74–84. https://doi.org/10.1016/j.cell.2008.07.044
13. Jalal ASB, Le TBK. Bacterial chromosome segregation by the ParABS system. *Open Biol* 2020;10:200097. https://doi.org/10.1098/rsob.200097
14. Tišma M, Kaljević J, Gruber S *et al.* Connecting the dots: key insights on ParB for chromosome segregation from single-molecule studies. *FEMS Microbiol Rev* 2024;48:1–13.
15. Mohl DA, Gober JW. Cell cycle-dependent polar localization of chromosome partitioning proteins in *Caulobacter crescentus*. *Cell* 1997;88:675–84. https://doi.org/10.1016/S0092-8674(00)81910-8
16. Ireton K, Gunther IV NW, Grossman AD. spo0J is required for normal chromosome segregation as well as the initiation of sporulation in *Bacillus subtilis*. *J Bacteriol* 1994;176:5320–9. https://doi.org/10.1128/jb.176.17.5320-5329.1994

17. Riley EP, Schwarz C, Derman AI *et al.* Milestones in *Bacillus subtilis* sporulation research. *Microb Cell* 2020;8:1–16. https://doi.org/10.15698/mic2021.01.739
18. Soh YM, Bürmann F, Shin HC *et al.* Molecular basis for SMC rod formation and its dissolution upon DNA binding. *Mol Cell* 2015;57:290–303. https://doi.org/10.1016/j.molcel.2014.11.023
19. Osorio-Valeriano M, Altegoer F, Steinchen W *et al.* ParB-type DNA segregation proteins are CTP-dependent molecular switches. *Cell* 2019;179:1512–24.e15. https://doi.org/10.1016/j.cell.2019.11.015
20. Osorio-Valeriano M, Altegoer F, Das CK *et al.* The CTPase activity of ParB determines the size and dynamics of prokaryotic DNA partition complexes. *Mol Cell* 2021;81:3992–4007.e10. https://doi.org/10.1016/j.molcel.2021.09.004
21. Jalal AS, Tran NT, Stevenson CE *et al.* A CTP-dependent gating mechanism enables ParB spreading on DNA. *eLife* 2021;10:e69676. https://doi.org/10.7554/eLife.69676
22. Szymczak J, Strzałka A, Bania D *et al.* Significance of the CTP-binding motif for the interactions of S. coelicolor ParB with DNA, chromosome segregation, and sporogenic hyphal growth. *Nucleic Acids Res* 2025;53:gkaf623. https://doi.org/10.1093/nar/gkaf623
23. Babl L, Giacomelli G, Ramm B *et al.* CTP-controlled liquid–liquid phase separation of ParB. *J Mol Biol* 2022;434:167401. https://doi.org/10.1016/j.jmb.2021.167401
24. Davis MA, Martin KA, Austin SJ. Biochemical activities of the parA partition protein of the P1 plasmid. *Mol Microbiol* 1992;6:1141–7. https://doi.org/10.1111/j.1365-2958.1992.tb01552.x
25. Radnedge L, Youngren B, Davis M *et al.* Probing the structure of complex macromolecular interactions by homolog specificity scanning: the P1 and P7 plasmid partition systems. *EMBO J* 1998;17:6076–85. https://doi.org/10.1093/emboj/17.20.6076
26. Schnabel L, Osorio-Valeriano M, Perez-Borrajero C *et al.* Molecular basis of ParA ATPase activation by the CTPase ParB during bacterial chromosome segregation. *Nat Commun* 2025;16:8428. https://doi.org/10.1038/s41467-025-63976-0
27. Zhao Y, Guo L, Hu J *et al.* Phase-separated ParB enforces diverse DNA compaction modes and stabilizes the parS-centered partition complex. *Nucleic Acids Res* 2024;52:8385–98. https://doi.org/10.1093/nar/gkae533
28. Leonard TA, Butler PJG, Löwe J. Structural analysis of the chromosome segregation protein Spo0J from *Thermus thermophilus*. *Mol Microbiol* 2004;53:419–32. https://doi.org/10.1111/j.1365-2958.2004.04133.x
29. Schumacher MA, Funnell BE. Structures of ParB bound to DNA reveal mechanism of partition complex formation. *Nature* 2005;438:516–9. https://doi.org/10.1038/nature04149
30. Soh YM, Davidson IF, Zamuner S *et al.* Self-organization of parS centromeres by the ParB CTP hydrolase. *Science* 2019;366:1129–33. https://doi.org/10.1126/science.aay3965
31. Chen B-W, Lin M-H, Chu C-H *et al.* Insights into ParB spreading from the complex structure of Spo0J and parS. *Proc Natl Acad Sci USA* 2015;112:6613–8. https://doi.org/10.1073/pnas.1421927112
32. Taylor JA, Pastrana CL, Butterer A *et al.* Specific and non-specific interactions of ParB with DNA: implications for chromosome segregation. *Nucleic Acids Res* 2015;43:719–31. https://doi.org/10.1093/nar/gku1295
33. Fisher GLM, Pastrana CL, Higman VA *et al.* The structural basis for dynamic DNA binding and bridging interactions which condense the bacterial centromere. *eLife* 2017;6:e28086. https://doi.org/10.7554/eLife.28086
34. Murray H, Ferreira H, Errington J. The bacterial chromosome segregation protein Spo0J spreads along DNA from parS nucleation sites. *Mol Microbiol* 2006;61:1352–61. https://doi.org/10.1111/j.1365-2958.2006.05316.x
35. Tran NT, Stevenson CE, Som NF *et al.* Permissive zones for the centromere-binding protein ParB on the *Caulobacter crescentus* chromosome. *Nucleic Acids Res* 2018;46:1196–209. https://doi.org/10.1093/nar/gkx1192
36. Rodionov O, ŁObocka M, Yarmolinsky M. Silencing of genes flanking the P1 plasmid centromere. *Science* 1999;283:546–9. https://doi.org/10.1126/science.283.5401.546
37. Jalal AS, Tran NT, Le TB. ParB spreading on DNA requires cytidine triphosphate *in vitro*. *eLife* 2020;9:1–24. https://doi.org/10.7554/eLife.53515
38. Graham TGW, Wang X, Song D *et al.* ParB spreading requires DNA bridging. *Genes Dev* 2014;28:1228–38. https://doi.org/10.1101/gad.242206.114
39. Sanchez A, Cattoni DI, Walter J-C *et al.* Stochastic self-assembly of ParB proteins builds the bacterial DNA segregation apparatus. *Cell Syst* 2015;1:163–73. https://doi.org/10.1016/j.cels.2015.07.013
40. Antar H, Soh Y-M, Zamuner S *et al.* Relief of ParB autoinhibition by parS DNA catalysis and recycling of ParB by CTP hydrolysis promote bacterial centromere assembly. *Sci Adv* 2021;7:esbj2854. https://doi.org/10.1126/sciadv.abj2854
41. Balaguer FA, Aicart-Ramos C, Fisher GL *et al.* CTP promotes efficient ParB-dependent DNA condensation by facilitating one-dimensional diffusion from parS. *eLife* 2021;10:e677554. https://doi.org/10.7554/eLife.67554
42. Guo L, Zhao Y, Zhang Q *et al.* Stochastically multimerized ParB orchestrates DNA assembly as unveiled by single-molecule analysis. *Nucleic Acids Res* 2022;50:9294–305. https://doi.org/10.1093/nar/gkac651
43. Molina M, Way LE, Ren Z *et al.* A framework to validate fluorescently labeled DNA-binding proteins for single-molecule experiments. *Cell Reports Methods* 2023;3:100614. https://doi.org/10.1016/j.crmeth.2023.100614
44. Cavanagh J, Fairbrother WJ, Palmer AGI *et al.* Protein NMR Spectroscopy. London, United Kingdom: Elsevier. 2007.
45. Vold RL, Waugh JS, Klein MP *et al.* Measurement of spin relaxation in complex systems. *J Chem Phys* 1968;48:3831–2. https://doi.org/10.1063/1.1669699
46. Meiboom S, Gill D. Modified spin-echo method for measuring nuclear relaxation times. *Rev Sci Instrum* 1958;29:688–91. https://doi.org/10.1063/1.1716296
47. Noggle JH, Schirmer RE. *The Nuclear Overhauser Effect: Chemical Applications*: Academic Press, New York, USA 1971.
48. Massi F, Johnson E, Wang C *et al.* NMR R1 rho rotating-frame relaxation with weak radio frequency fields. *J Am Chem Soc* 2004;126:2247–56. https://doi.org/10.1021/ja038721w
49. Davis DG, Perlman ME, London RE. Direct measurements of the dissociation-rate constant for inhibitor-enzyme complexes via the T_1 rho and T_2 (CPMG) methods. *J Magn Reson B* 1994;104:266–75. https://doi.org/10.1006/jmrb.1994.1084
50. Kay LE, Torchia DA, Bax A. Backbone dynamics of proteins as studied by nitrogen-15 inverse detected heteronuclear NMR spectroscopy: application to staphylococcal nuclease. *Biochemistry* 1989;28:8972–9. https://doi.org/10.1021/bi00449a003
51. Kay LE, Nicholson LK, Delaglio F *et al.* Pulse sequences for removal of the effects of cross correlation between dipolar and chemical-shift anisotropy relaxation mechanisms on the measurement of heteronuclear T_1 and T_2 values in proteins. *J Magn Reson* 1992;97:359–75. https://doi.org/10.1016/0022-2364(92)90320-7
52. Barbato G, Ikura M, Kay LE *et al.* Backbone dynamics of calmodulin studied by nitrogen-15 relaxation using inverse detected two-dimensional NMR spectroscopy: the central helix is flexible. *Biochemistry* 1992;31:5269–78. https://doi.org/10.1021/bi00138a005
53. Palmer AG, Skelton NJ, Chazin WJ *et al.* Suppression of the effects of cross-correlation between dipolar and anisotropic chemical shift relaxation mechanisms in the measurement of spin–spin relaxation rates. *Mol Phys* 1992;75:699–711. https://doi.org/10.1080/00268979200100511

54. Delaglio F, Grzesiek S, Vuister GW *et al.* NMRPipe: a multidimensional spectral processing system based on UNIX pipes. *J Biomol NMR* 1995;6:277–93. https://doi.org/10.1007/BF00197809
55. Lee LK, Rance M, Chazin WJ *et al.* Rotational diffusion anisotropy of proteins from simultaneous analysis of 15N and 13Cα nuclear spin relaxation. *J Biomol NMR* 1997;9:287–98. https://doi.org/10.1023/A:1018631009583
56. Clore GM, Driscoll PC, Wingfield PT *et al.* Analysis of the backbone dynamics of interleukin-1 beta using two-dimensional inverse detected heteronuclear 15N-1H NMR spectroscopy. *Biochemistry* 1990;29:7387–401. https://doi.org/10.1021/bi00484a006
57. Tjandra N, Feller SE, Pastor RW *et al.* Rotational diffusion anisotropy of human ubiquitin from 15N NMR relaxation. *J Am Chem Soc* 1995;117:12562–6. https://doi.org/10.1021/ja00155a020
58. Tjandra N, Garrett DS, Gronenborn AM *et al.* Defining long range order in NMR structure determination from the dependence of heteronuclear relaxation times on rotational diffusion anisotropy. *Nat Struct Mol Biol* 1997;4:443–9. https://doi.org/10.1038/nsb0697-443
59. Cole R, Loria JP. FAST-Modelfree: a program for rapid automated analysis of solution NMR spin-relaxation data. *J Biomol NMR* 2003;26:203–13. https://doi.org/10.1023/A:1023808801134
60. Lipari G, Szabo A. Model-free approach to the interpretation of nuclear magnetic resonance relaxation in macromolecules. 1. Theory and range of validity. *J Am Chem Soc* 1982;104:4546–59. https://doi.org/10.1021/ja00381a009
61. Mandel AM, Akke M, Palmer III A.G. Backbone dynamics of *Escherichia coli* ribonuclease HI: correlations with structure and function in an active enzyme. *J Mol Biol* 1995;246:144–63. https://doi.org/10.1006/jmbi.1994.0073
62. Palmer III AG, Cavanagh J, Wright PE *et al.* Sensitivity improvement in proton-detected two-dimensional heteronuclear correlation NMR spectroscopy. *J Magn Reson* 1991;93:151–70. https://doi.org/10.1016/0022-2364(91)90036-S
63. Jarymowycz VA, Stone MJ. Fast time scale dynamics of protein backbones: NMR relaxation methods, applications, and functional consequences. *Chem Rev* 2006;106:1624–71. https://doi.org/10.1021/cr040421p
64. Kim H, Loparo JJ. Observing bacterial chromatin protein–DNA interactions by combining DNA flow-stretching with single-molecule imaging. *Methods Mol Biol* 2018;1837:277–99.
65. Edelstein AD, Tsuchida MA, Amodaj N *et al.* Advanced methods of microscope control using μManager software. *J Biol Methods* 2014;1:1. https://doi.org/10.14440/jbm.2014.36
66. Schindelin J, Arganda-Carreras I, Frise E *et al.* Fiji: an open-source platform for biological-image analysis. *Nat Methods* 2012;9:676–82. https://doi.org/10.1038/nmeth.2019
67. Kim H, Loparo JJ. Multistep assembly of DNA condensation clusters by SMC. *Nat Commun* 2016;7:1–12.
68. Abraham MJ, Murtola T, Schulz R *et al.* GROMACS: high performance molecular simulations through multi-level parallelism from laptops to supercomputers. *SoftwareX* 2015;1–2:19–25. https://doi.org/10.1016/j.softx.2015.06.001
69. Abramson J, Adler J, Dunger J *et al.* Accurate structure prediction of biomolecular interactions with AlphaFold 3. *Nature* 2024;630:493–500. https://doi.org/10.1038/s41586-024-07487-w
70. Hornak V, Abel R, Okur A *et al.* Comparison of multiple Amber force fields and development of improved protein backbone parameters. *Proteins* 2006;65:712–25. https://doi.org/10.1002/prot.21123
71. Jorgensen WL, Chandrasekhar J, Madura JD *et al.* Comparison of simple potential functions for simulating liquid water. *J Chem Phys* 1983;79:926–35. https://doi.org/10.1063/1.445869
72. Essmann U, Perera L, Berkowitz ML *et al.* A smooth particle mesh Ewald method. *J Chem Phys* 1995;103:8577–93. https://doi.org/10.1063/1.470117
73. Bussi G, Donadio D, Parrinello M. Canonical sampling through velocity rescaling. *J Chem Phys* 2007;126:014101. https://doi.org/10.1063/1.2408420
74. Bernetti M, Bussi G. Pressure control using stochastic cell rescaling. *J Chem Phys* 2020;153:114107. https://doi.org/10.1063/5.0020514
75. Hess B, Bekker H, Berendsen HJC *et al.* LINCS: a linear constraint solver for molecular simulations. *J Comput Chem* 1997;18:1463–72. https://doi.org/10.1002/(SICI)1096-987X(199709)18:12⟨1463::AID-JCC4⟩3.0.CO;2-H
76. Bowman GR. Accurately modeling nanosecond protein dynamics requires at least microseconds of simulation. *J Comput Chem* 2016;37:558–66. https://doi.org/10.1002/jcc.23973
77. Harwood CR, Cutting SM. *Molecular Biological Methods for Bacillus Wiley*. New York, USA: Wiley. 1990.
78. Wang X, Montero Llopis P. Visualizing *Bacillus subtilis* during vegetative growth and spore formation. *Methods Mol Biol* 2016;1431:275–87.
79. Sapienza PJ, Lee AL. Using NMR to study fast dynamics in proteins: methods and applications. *Curr Opin Pharmacol* 2010;10:723–30. https://doi.org/10.1016/j.coph.2010.09.006
80. Song D, Rodrigues K, Graham TGW *et al.* A network of cis and trans interactions is required for ParB spreading. *Nucleic Acids Res* 2017;45:7106–17. https://doi.org/10.1093/nar/gkx271
81. Case DA. Molecular dynamics and NMR spin relaxation in proteins. *Acc Chem Res* 2002;35:325–31. https://doi.org/10.1021/ar010020l
82. Hornak V, Abel R, Okur A *et al.* Comparison of multiple Amber force fields and development of improved protein backbone parameters. *Proteins* 2006;65:712–25. https://doi.org/10.1002/prot.21123
83. Williamson MP. Using chemical shift perturbation to characterise ligand binding. *Prog Nucl Magn Reson Spectrosc* 2013;73:1–16. https://doi.org/10.1016/j.pnmrs.2013.02.001
84. Shehzad S, Kim H. Single-molecule DNA-flow stretching assay as a versatile hybrid tool for investigating DNA-protein interactions. *BMB Rep* 2025;58:41–51. https://doi.org/10.5483/BMBRep.2024-0177
85. Tišma M, Panoukidou M, Antar H *et al.* ParB proteins can bypass DNA-bound roadblocks via dimer-dimer recruitment. *Sci Adv* 2022;8:esbn3299.
86. Broedersz CP, Wang X, Meir Y *et al.* Condensation and localization of the partitioning protein ParB on the bacterial chromosome. *Proc Natl Acad Sci USA* 2014;111:8809–14. https://doi.org/10.1073/pnas.1402529111
87. Walter J-C, Walliser N-O, David G *et al.* Looping and clustering model for the organization of protein–DNA complexes on the bacterial genome. *New J Phys* 2018;20:035002. https://doi.org/10.1088/1367-2630/aaad39
88. Merino Urteaga R, Ha T. Mind your tag in single-molecule measurements. *Cell reports methods* 2023;3:100623. https://doi.org/10.1016/j.crmeth.2023.100623
89. Sharpe ME, Errington J. The *Bacillus subtilis* soj-spo0J locus is required for a centromere-like function involved in prespore chromosome partitioning. *Mol Microbiol* 1996;21:501–9. https://doi.org/10.1111/j.1365-2958.1996.tb02559.x
90. Lin DCH, Levin PA, Grossman AD. Bipolar localization of a chromosome partition protein in *Bacillus subtilis*. *Proc Natl Acad Sci USA* 1997;94:4721–6. https://doi.org/10.1073/pnas.94.9.4721
91. Webb CD, Teleman A, Gordon S *et al.* Bipolar localization of the replication origin regions of chromosomes in vegetative and sporulating cells of *B. subtilis*. *Cell* 1997;88:667–74. https://doi.org/10.1016/S0092-8674(00)81909-1

92. Autret S, Nair R, Errington J. Genetic analysis of the chromosome segregation protein Spo0J of *Bacillus subtilis*: evidence for separate domains involved in DNA binding and interactions with Soj protein. *Mol Microbiol* 2001;41:743–55. https://doi.org/10.1046/j.1365-2958.2001.02551.x
93. Henzler-Wildman K, Kern D. Dynamic personalities of proteins. *Nature* 2007;450:964–72. https://doi.org/10.1038/nature06522
94. Kalodimos CG, Biris N, Bonvin AMJJ *et al*. Structure and flexibility adaptation in nonspecific and specific protein–DNA complexes. *Science* 2004;305:386–9. https://doi.org/10.1126/science.1097064
95. Sullivan SM, Maddock JR. Bacterial sporulation: pole-to-pole protein oscillation. *Curr Biol* 2000;10:R159–61. https://doi.org/10.1016/S0960-9822(00)00331-6
96. Marston AL, Errington J. Dynamic movement of the ParA-like Soj protein of B. subtilis and its dual role in nucleoid organization and developmental regulation. *Mol Cell* 1999;4:673–82. https://doi.org/10.1016/S1097-2765(00)80378-0
97. Moldovan G-L, Pfander B, Jentsch S. PCNA, the maestro of the replication fork. *Cell* 2007;129:665–79. https://doi.org/10.1016/j.cell.2007.05.003
98. Krishna TS, Kong XP, Gary S *et al*. Crystal structure of the eukaryotic DNA polymerase processivity factor PCNA. *Cell* 1994;79:1233–43. https://doi.org/10.1016/0092-8674(94)90014-0
99. Gulbis JM, Kelman Z, Hurwitz J *et al*. Structure of the C-terminal region of p21(WAF1/CIP1) complexed with human PCNA. *Cell* 1996;87:297–306. https://doi.org/10.1016/S0092-8674(00)81347-1
100. De March M, Merino N, Barrera-Vilarmau S *et al*. Structural basis of human PCNA sliding on DNA. *Nat Commun* 2017;8:13935. https://doi.org/10.1038/ncomms13935
101. Wing R, Drew H, Takano T *et al*. Crystal structure analysis of a complete turn of B-DNA. *Nature* 1980;287:755–8. https://doi.org/10.1038/287755a0
102. Fukuda K, Morioka H, Imajou S *et al*. Structure-function relationship of the eukaryotic DNA replication factor, proliferating cell nuclear antigen. *J Biol Chem* 1995;270:22527–34. https://doi.org/10.1074/jbc.270.38.22527
103. Zhou Y, Hingorani MM. Impact of individual proliferating cell nuclear antigen-DNA contacts on clamp loading and function on DNA. *J Biol Chem* 2012;287:35370–81. https://doi.org/10.1074/jbc.M112.399071

Received: July 10, 2025. **Revised:** February 16, 2026. **Accepted:** February 17, 2026